Precambrian Research 403 (2024) 107301

Contents lists available at ScienceDirect

Precambrian Research

journal homepage: www.elsevier.com/locate/precamres

Petrogenesis of the Neoproterozoic Fanjingshan leucogranite associated with W–Sn mineralization: Insights from U–Pb ages and geochemistry

Xiao-Yan Jiang [a], Jia Guo [b], Wei-Guang Zhu [a,*], Jin-Cheng Luo [a], Ke-Nan Jiang [a,c]

[a] State Key Laboratory of Ore Deposit Geochemistry, Institute of Geochemistry, Chinese Academy of Sciences, Guiyang 550081, China
[b] College of Earth Sciences, Chengdu University of Technology, Chengdu 610059, China
[c] University of Chinese Academy of Sciences, Beijing, China

ARTICLE INFO

Keywords:
Leucogranite
Accessory minerals
W–Sn mineralization
Jiangnan Orogen
Fanjingshan

ABSTRACT

The Jiangnan Orogen in China host large volumes of Neoproterozoic igneous rocks and is a well-preserved Neoproterozoic orogenic belt in the South China Block. A series of W–Sn mineralization occurrences and ore deposits are spatially related to Neoproterozoic granites in the orogen. However, the geochronology and petrogenesis of the host Neoproterozoic granites and associated W–Sn mineralization in the western Jiangnan Orogen remain poorly understood. In this study, the U–Pb ages of zircon, cassiterite, and apatite, and the geochemistry of minerals and whole rock of the Fanjingshan (FJS) leucogranites, which are located along the western margin of the Jiangnan Orogen, were used to re-evaluate the Neoproterozoic magmatism that occurred in response to the orogeny and the mechanism of W–Sn mineralization. The FJS leucogranites consist mainly of strongly peraluminous tourmaline–muscovite granites. The leucogranites have a characteristic magmatic and hydrothermal mineral assemblage, including cassiterite, tourmaline and fluorite. Zircon U–Pb dating indicates the leucogranites were emplaced at *ca.* 812 Ma, which is consistent with apatite U–Pb age. Cassiterite U–Pb dating yields an age of *ca.* 810 Ma, suggesting the mineralization was coeval with the crystallization of the FJS leucogranites. In multi-element variation diagrams, all samples display sea-gull-shaped rare earth element patterns with significant negative Eu anomalies. The whole-rock geochemical data suggest the leucogranites originated by muscovite dehydration melting of a metasedimentary source. Extensive fractional crystallization and magmatic–hydrothermal interactions, as inferred from extremely low rare earth element contents, low Nb/Ta and Zr/Hf ratios, and a large tetrad effect, lead to the W–Sn enrichment and crystallization of ore minerals, such as cassiterite and scheelite. The compositions of muscovite, apatite, cassiterite and tourmaline, along with the occurrence of quartz veins, also provide information on the nature of the magmatic–hydrothermal processes and mineralization. Our data and those for other S-type granites (840–800 Ma) in the western Jiangnan Orogen, suggest that magmatic–hydrothermal processes had a key role in W–Sn mineralization. The Neoproterozoic FJS leucogranites likely formed in an extensional setting during the final stage of orogenesis.

1. Introduction

Granites are essential components of the continental crust and are dominantly the products of crustal anatexis (Chappell, 2004; Wu et al., 2017; Zheng and Gao, 2021). The geochronology and petrogenesis of granites are important for understanding the evolution of the continental crust (Collins, 1996). Granitic melts are subjected to extensive magmatic differentiation by fractional crystallization and intense interaction with aqueous hydrothermal fluids. These processes have an important role in various types of mineralization (Jahn et al., 2001; Lee and Morton, 2015). In particular, leucogranites (high SiO_2 contents and low contents of mafic minerals [<5 vol%]) are economically important and can host rare metal mineralization (Garcia-Arias, 2020; Cao et al., 2022). However, the sources of leucogranites are debated. They have been proposed to be derived by melting of purely sediments (Le Fort et al., 1987; Gao et al., 2016; Shakerardakani et al., 2020; Sylvester, 1998), or generated from multiple crustal sources, with or without inputs from mantle-derived melts (Wu et al., 2020; Tian et al., 2017; Wang et al., 2017).

Tungsten and Sn are critical metals for high-technology industries, and are also used in the low-C economy. The South China Block (SCB) hosts multi-stage granites and large-scale metal deposits, containing >

* Corresponding author.
E-mail address: zhuweiguang@mail.gyig.ac.cn (W.-G. Zhu).

https://doi.org/10.1016/j.precamres.2024.107301
Received 26 May 2023; Received in revised form 24 December 2023; Accepted 20 January 2024
Available online 6 February 2024

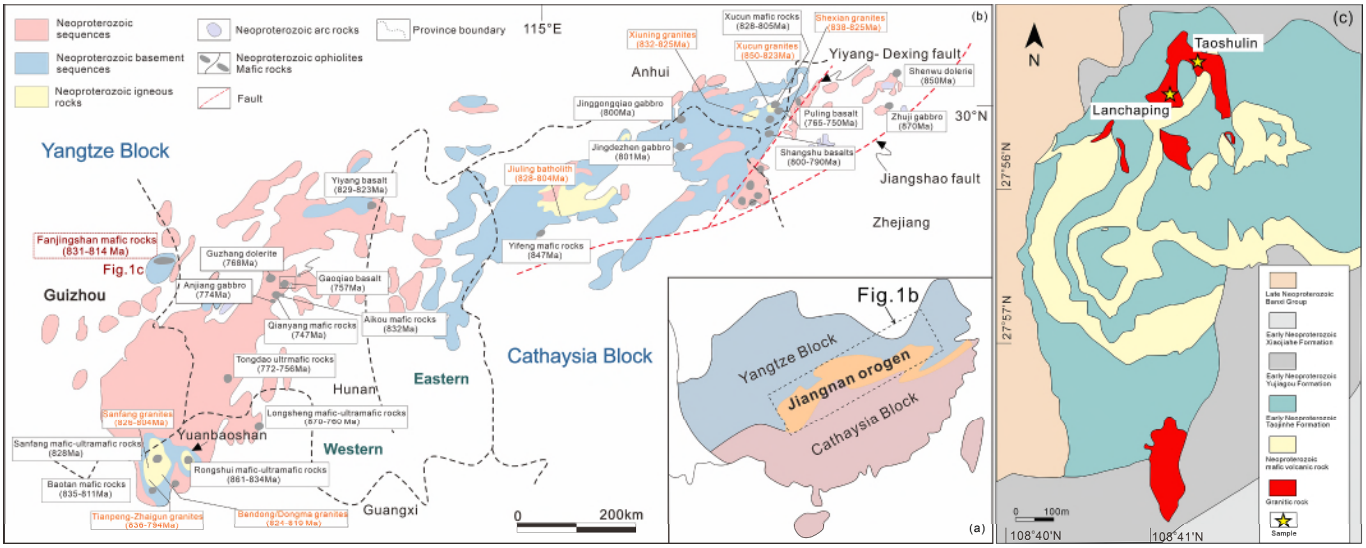

Fig. 1. (a) Sketch map showing the major tectonic units of the South China Block. (b) Distribution of Neoproterozoic magmatic rocks in the Jiangnan Orogen (modified from Wang et al., 2014, Kou et al., 2018; Wan et al., 2021); (c) Geological map of the FJS area, showing sampling locations (modified after Lv et al., 2021).

50 % of global W reserves and 20 % of global Sn reserves (Mao et al., 2013; Zhao et al., 2017). The W–Sn mineralization in the SCB, occurred during the Neoproterozoic, Early Paleozoic, and Mesozoic (Guo et al., 2018; Huang et al., 2023; Mao et al., 2013, 2021; Xiang et al., 2020; Zhang et al., 2021a). Most W–Sn deposits have close spatial–temporal association with highly evolved granites (Romer and Kroner, 2016; Yuan et al., 2018). The ore-forming elements of W–Sn deposits are concentrated in enriched melt (Hedenquist and Lowenstern, 1994). Oxygen fugacity has a significant effect on the contents of ore-forming elements and the mineralization type of the granitic magma (Ballard et al., 2002; Li et al., 2017; Richards, 2015). Magmatic differentiation is also important for the enrichment of W–Sn (Blevin and Chappell, 1995; Breiter, 2012; Xu et al., 2015). As such, W–Sn mineralization is controlled by the magma source, conditions of partial melting, and magmatic differentiation of ore-bearing granitic magma (Ishihara, 1981; Romer and Kroner, 2016; Zhang et al., 2019). The relationship between mineralization and granites is critical for discovering economic W–Sn ore deposits. Therefore, the petrogenesis of Neoproterozoic granites and associated W–Sn mineralization in the SCB require further investigation.

Accessory minerals in granitic rocks can preserve information regarding source components, magmatic evolution, and mineralization processes, which can provide insights into the petrogenesis of their host magma and mineralization mechanisms. Apatite is ubiquitous in granite and is early crystallizing. The geochemical compositions of apatite have been used for a wide range of research applications, including geochronology, and the determination of physico-chemical conditions and magmatic processes (Harrison and Watson, 1984; Hoskin and Ireland, 2000; Harlov, 2015; Jiang et al., 2018; Andersson et al., 2019; Resentini et al., 2020). The timing of mineralization constrains the origins and history of ore formation (Stein et al., 1997; Yuan et al., 2008; Chiaradia et al., 2009; Li et al., 2010). Cassiterite (SnO_2) is the main ore mineral in Sn deposits, and the U–Pb system can remain closed during post-ore hydrothermal alteration and weathering. As such, cassiterite is suitable for U–Pb dating and is increasingly used to provide precise and accurate age constraints on Sn–W mineralization (Yuan et al., 2008, 2011; Zhang et al., 2017a, 2017b; Guo et al., 2018). Tourmaline is a common borosilicate mineral in granitic rocks and related hydrothermal systems and is often associated with W–Sn deposits (Slack, 1996; Slack and Trumbull, 2011; Zhang et al., 2021a; Guo et al., 2022). It records magmatic–hydrothermal processes related to W–Sn mineralization and is also a tool for mineral exploration (London and Manning, 1995; Jiang et al., 2008; Drivenes et al., 2015; Zhao et al., 2021a; Zhao et al., 2021b). Therefore, the accessory minerals in granitic rocks can provide key information on their petrogenesis and related mineralization.

The Yangtze and Cathaysia blocks were amalgamated during the Neoproterozoic and to form the Jiangnan Orogen. This was a significant event in the Precambrian magmatic and crustal evolution of the SCB (Li et al., 2009a; Zhao and Cawood, 2012; Zhou et al., 2002), and had a role in the generation of abundant igneous rocks in the Jiangnan Orogen with ages of 870–750 Ma (Kou et al., 2018, 2021; Li et al., 1999; Xue et al., 2012; Wang et al., 2014a; Wan et al., 2021; Zhou et al., 2009). The Jiangnan Orogen can be divided into a western part, located mainly in Hunan–Guizhou–Guangxi provinces, and an eastern part (Guo and Gao, 2018; Wang et al., 2014a; Fig. 1). The scarcity of igneous rocks in the western part of the orogeny means that their geochronological framework and origin remain poorly known. Neoproterozoic peraluminous granites are exposed in the Fanjingshan (FJS) region along the southwestern margin of the Jiangnan Orogen, spatially associated with W–Sn mineralization. Neoproterozoic W–Sn mineralization related to the FJS granites was discovered almost four decades ago (Xia, 1985), and is suggested to be of granite-related hydrothermal origin (Lv et al., 2021; Xiang et al., 2020). Although the mineralization has been studied, the link between mineralization and the FJS granites requires further research. This study examined representative samples of the FJS leucogranites and related W–Sn mineralization in Guizhou Province, western Jiangnan Orogen. Cassiterite U–Pb dating was undertaken to determine the age of mineralization. Zircon and apatite U–Pb ages of the leucogranites were used to establish the temporal relationship between the granitic magmatism and W–Sn mineralization. Building on these age data, apatite, cassiterite and tourmaline geochemistry, and whole-rock geochemical analyses were used to constrain the petrogenesis of the leucogranites and determine the key controls on Neoproterozoic mineralization in the Jiangnan Orogen.

2. Geological setting

The SCB, which consists of the Yangtze and the Cathaysia blocks (Fig. 1a) is separated from the Songpan–Ganzi Terrane (SGT) to the west by Late Triassic to Early Jurassic thrust belts, and from the North China Craton by the Permian–Triassic Qinling–Dabie–Sulu (QDS) Orogen. During the Neoproterozoic, in the terminal stage of the Rodinia supercontinent cycle, collisions between continental blocks, formed the nearly NE–SW trending, 1500-km-long and 80–120-km-wide Jiangnan Orogen, which comprises upper Mesoproterozoic to lower Neoproterozoic volcanic–sedimentary sequences (Fig. 1; Cawood et al., 2013, 2018; Wang et al., 2019; Yao et al., 2017; Zhao and Cawood,

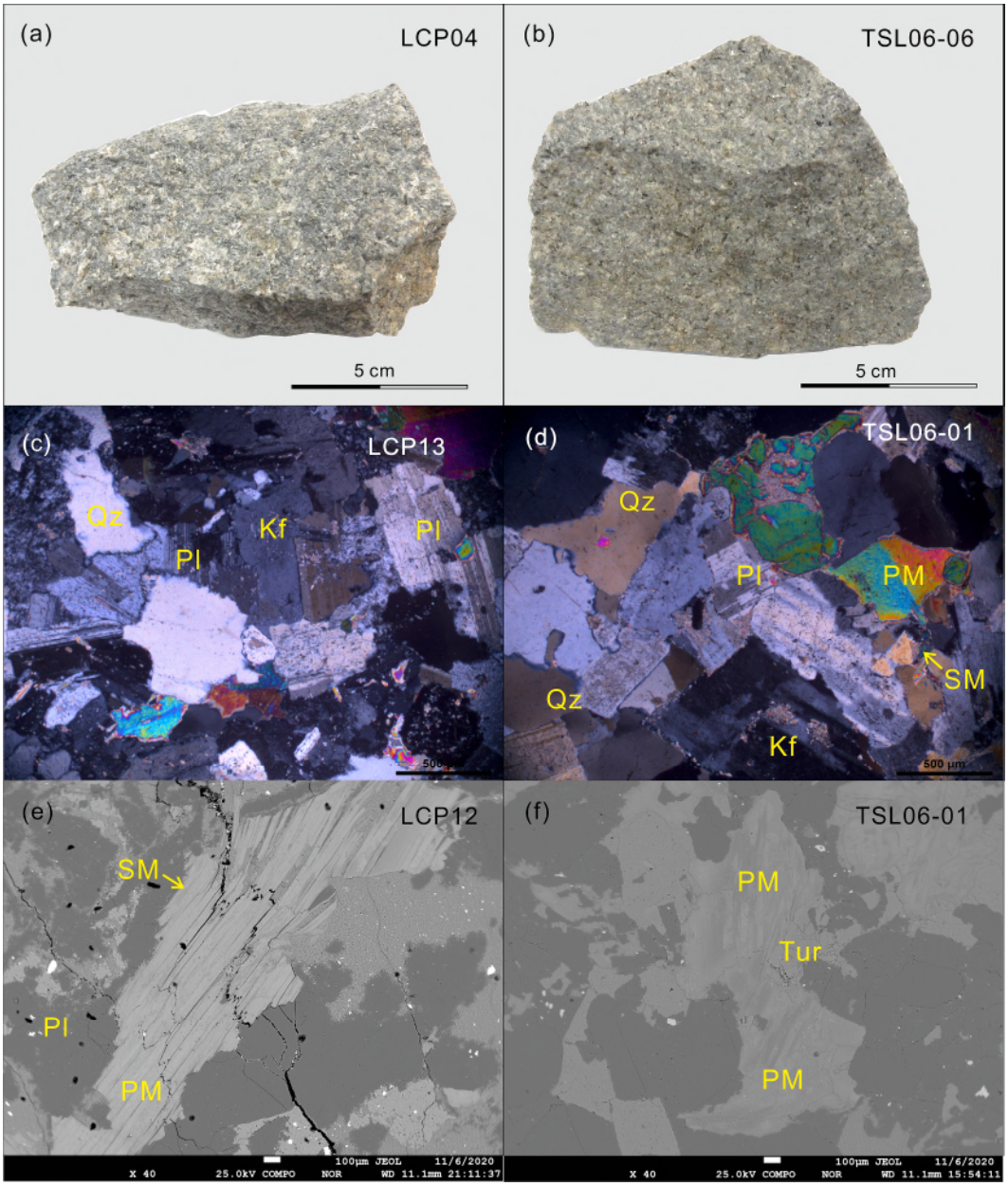

Fig. 2. Photographs and micrographs of leucogranites from the FJS region. (a–b) Photographs of hand specimens; (c–f) Petrographic characteristics of the leucogranites. Qz = quartz, Kf = K-feldspar, Pl = plagioclase, PM = primary muscovite, SM = secondary muscovite, Tur = tourmaline.

2012). The western part of the orogeny contains dikes and sills of Neoproterozoic mafic–ultramafic rocks (870–750 Ma), mainly basalt, gabbro, diabase, and olivine pyroxenite (Chen et al., 2018; Shu et al., 2019; Wan et al., 2021; Wang et al., 2012; Wang et al., 2019; Xue et al., 2012; Yao et al., 2019; Zhou et al., 2009). It also contains granitoids, such as the Fanjingshan, Sanfang, Bendong, Motianling, and Yuanbaoshan plutons, which are primarily granodiorite, monzonitic granite, two-mica granite, and leucogranite (Li et al., 2003; Shu et al., 2021; Wang et al., 2017; Wang et al., 2004, 2006, 2014b; Yan et al., 2021; Yao et al., 2014; Zheng et al., 2007, 2008). The basement rocks of the study area are dominated by metamorphosed sandy-argillaceous rocks of the FJS Group (maximum depositional age of 870–830 Ma; Zhou et al., 2009; Zhao et al., 2011; Zhao et al., 2018). The FJS Group has been intruded by silicic plutons of muscovite granite and granitic pegmatite, and mafic–ultramafic plutons/dikes of gabbro, diabase, and olivine pyroxenite (Xue et al., 2012; Wang et al., 2011a,b; Zhao et al., 2018). All of these plutons are unconformably overlain by *meta*-siltstone and phyllite of the Xiajiang–Danzhou groups (maximum depositional age of 800–750 Ma; Zhao et al., 2018).

The FJS pluton covers an area of ~ 15 km^2 at Taoshulin (TSL), Lanchaping (LCP) and Xiaojiahe (Fig. 1c). These silicic intrusions are predominantly undeformed, medium- to fine-grained massive tourmaline–muscovite leucogranite with an equigranular texture. Minor pegmatites occur locally at the margins of the leucogranites. Regional NE–SW-trending faults cut the sedimentary and mafic igneous rocks, and are locally mineralized in the form of tourmaline–quartz veins in diabase or metamorphosed sandstone. The veins are up to ~ 3 m wide and 600 m long, and contain minor disseminated cassiterite, wolframite, scheelite, and sulfide minerals (Xiang et al., 2020).

Twenty-three representative samples of leucogranites were collected from the TSL and LCP areas. The granites consist of quartz (30–35 vol%), plagioclase (35–40 vol%), alkali feldspar (15–25 vol%), muscovite (<8 vol%) and tourmaline (2 vol%) (Fig. 2). Plagioclase preserves typical polysynthetic twins (Fig. 2). Alkali feldspar is generally smaller in size

than plagioclase, and muscovite is relatively fresh. Accessory minerals have a heterogeneous distribution, and include zircon, apatite, cassiterite, scheelite, fluorite, and monazite.

3. Analytical methods

3.1. Cathodoluminescence imaging and mineral chemical analysis

Accessory minerals examined in this study were separated from bulk samples using by conventional rock crushing to 200 μm, followed by heavy liquid and magnetic separation. Selected grains were then mounted in epoxy resin and polished to expose grain cores. Before U–Pb dating and trace element analysis, zircon, apatite, cassiterite and tourmaline grains were carefully checked under a microscope to examine their internal structures (cracks and mineral/fluid inclusions) to guide the U–Pb isotope and trace element analyses. Backscattered electron (BSE) and cathodoluminescence (CL) imaging were undertaken using a JSM-7800F emission scanning electron microscope (SEM) coupled to a CL detector at the State Key Laboratory of Ore Deposit Geochemistry (SKLODG), Institute of Geochemistry, Chinese Academy of Sciences (IGCAS).

Major and minor element compositions of apatite and cassiterite were determined using a JEOL-1600 electron microprobe analyzer (EMPA) at the SKLODG, IGCAS. The analytical conditions for apatite were an accelerating voltage of 25 kV, a beam current of 10nA, and a beam diameter of 10 μm. A counting time of 20 s was used for most elements, with 40 s for F and 10 s for P and Ca. For tourmaline, analyses were performed with an accelerating voltage of 15 kV, beam current of 20nA, and beam diameter of 5 μm. The peak counting times were 10 s for Na, Mg, Al, Si, K, and Fe, and 20 s for Ti, Mn, Ca, F, and Cl. Other minerals, such as muscovite and feldspar, were analyzed with a beam diameter of 5 μm, accelerating voltage of 15 kv, and beam current of 10nA. The peak counting time for all elements was 10 s.

Well-characterized oxide and natural silicate minerals were used as standards for calibration. All data acquired during this study were corrected using standard ZAF correction procedures (Jurek and Hulínský, 1980). The analytical results and formulae of minerals in the leucogranites are listed in Supplementary Table 1.

3.2. Zircon U–Pb dating

Zircon grains and the zircon standard Temora were mounted in epoxy resin and polished to expose crystal cores for analysis. Zircon U–Pb dating was undertaken using a Cameca IMS-1280 ion microprobe at the Institute of Geology and Geophysics, Chinese Academy of Sciences (IGGCAS). The analytical procedures followed Li et al. (2009b). The analytical spot size was 20 × 30 μm. The U–Th–Pb isotope ratios were determined relative to the standard zircon Temora (Black et al., 2003). Measured Pb isotopic compositions were corrected for common Pb using the ^{204}Pb-method. Corrections are sufficiently small to be sensitive to the choice of common Pb composition because the measured ^{206}Pb/^{204}Pb ratios are mostly > 10,000. The average present-day crustal composition (Stacey and Kramers, 1975) was used for common Pb correction, assuming that the common Pb is largely surface contamination introduced during sample preparation. Uncertainties on individual analyses are reported at the 1σ level, and mean ages are quoted at the 95 % confidence levels. Data reduction was performed using Isoplot/Ex v.3.0 (Ludwig, 2003). The results of zircon U–Pb dating for the selected sample are presented in Supplementary Table 2.

3.3. Accessory mineral U–Pb dating and trace element analysis

In situ accessory minerals U–Pb dating and trace elemental analyses were undertaken at the SKLODG, IGCAS. Laser sampling was conducted using a GeoLasPro 193 nm ArF excimer laser. An Agilent 7900 ICP–MS (Inductively coupled plasma-Mass Spectrometry) was used to acquire the ion signal intensities. Helium was used as a carrier gas to enhance the transport efficiency of the ablated material. All reference materials were analyzed at the beginning of each session and after every 10 unknowns using the same conditions as for the samples. Each analysis began with a 20 s background acquisition followed by sample data acquisition of 40 s with the laser switched on.

For apatite dating, Durango apatite was used as the primary reference material, and Qinghu apatite (an in-house reference material) was used to monitor data quality. Apatite analyses used a laser beam diameter of 50 μm, laser frequency of 8 Hz, and a laser energy density of ~ 3.6 J/cm^2. Cassiterite analyses used a laser beam diameter of 60 μm, with laser energy density on the mineral surface of ~ 4 J/cm^2 and a repetition frequency of 6 Hz. NIST SRM610 and an in-house cassiterite standard (KA) were used for external elemental and isotopic calibration, respectively. The analytical procedures were similar to those described by Zhang et al., (2017a, 2017b). Trace element contents of tourmaline were determined using the NIST SRM 610 glass standard for external standardization and ^{29}Si as an internal standard. Tourmaline was ablated with a laser beam diameter of 30 μm at 8 Hz with energy of ~ 4 J/cm^2.

Offline data processing was undertaken using ICPMSDataCal software (Liu et al., 2010). The Concordia diagrams, weighted-mean ^{206}Pb/^{238}U ages, and Tera–Wasserburg diagrams for cassiterite and apatite were obtained using Isoplot 4.15 (Ludwig, 2012). The accuracy and precision of the laser ablation (LA) ICP–MS analyses are reported for international standards, including NIST SRM610 (Gao et al., 2002). The precision of the analyses of NIST SRM610 in this study is better than 2.5 % for trace elements. The limits of detection for most trace elements are well below the parts per million level. The U–Pb dating and trace elements results for selected samples are presented in Supplementary Table 3.

3.4. Whole-rock geochemical analyses

Whole-rock geochemical analyses for 23 granite samples were carried out at the SKLODG, IGCAS. Major elements were measured using a Thermo Fisher ARL Perform'X 4200 X-ray fluorescence (XRF) spectrometer on fused glass beads. The accuracy of the XRF analyses is estimated to be < 2 % for elements with contents of > 0.5 wt% and 5 % for those with contents of > 0.1 wt%. A Plasma Quantt-MS Elite ICP–MS was used for the determination of trace elements. The signal drift of the spectrometer was monitored with an internal Rh standard solution. Analytical uncertainties of the ICP–MS analyses are generally better than ± 5 % for most trace elements with contents of > 10 ppm and ± 10 % for other elements (<10 ppm). The operational and calibration procedures for the trace element analyses are similar to those detailed by Qi and Grégoire (2000). Major and trace element analyses are listed in Supplementary Table 4.

The Sm–Nd isotope analyses followed the procedures of Yang et al. (2011). The whole-rock powders were dissolved in HF + HNO_3 + $HClO_4$ in Teflon screw-top capsules. Samarium and Nd were separated using the classical two-step ion exchange chromatographic method and analyzed on a Thermo Scientific Neptune multiple-collector ICPMS. The total procedural blanks were < 50 pg for Nd. Measured Nd isotope ratios were normalized to ^{146}Nd/^{144}Nd = 0.7219. In the course of this study, analysis of the JNdi-1 Nd standard yielded ^{143}Nd/^{144}Nd = 0.512103 ± 12 (2SD, n = 3). USGS reference material BCR-2 was also analyzed for Nd isotopes and yielded ^{143}Nd/^{144}Nd = 0.512635 ± 9. Whole-rock Nd isotope data are given in Supplementary Table 4.

4. Results

4.1. Mineral chemistry

4.1.1. Muscovite

Muscovite in the FJS leucogranites can be divided into primary and

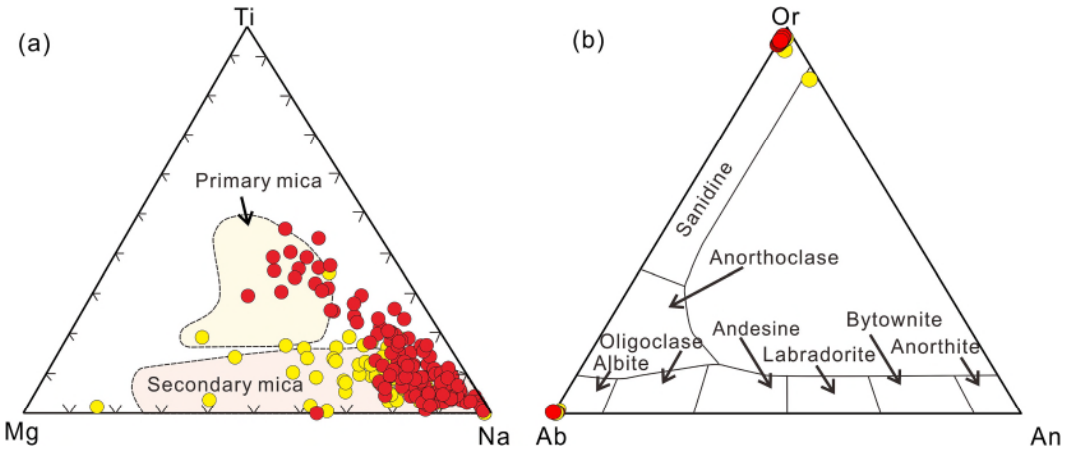

Fig. 3. Geochemical compositions of rock-forming minerals in the FJS leucogranites. (a) Classification diagram in terms of Ti, Mg, and Na (Miller et al., 1981) for discrimination between primary and secondary muscovite. (b) Anorthite–albite–orthoclase ternary plot for plagioclase and alkali feldspar.

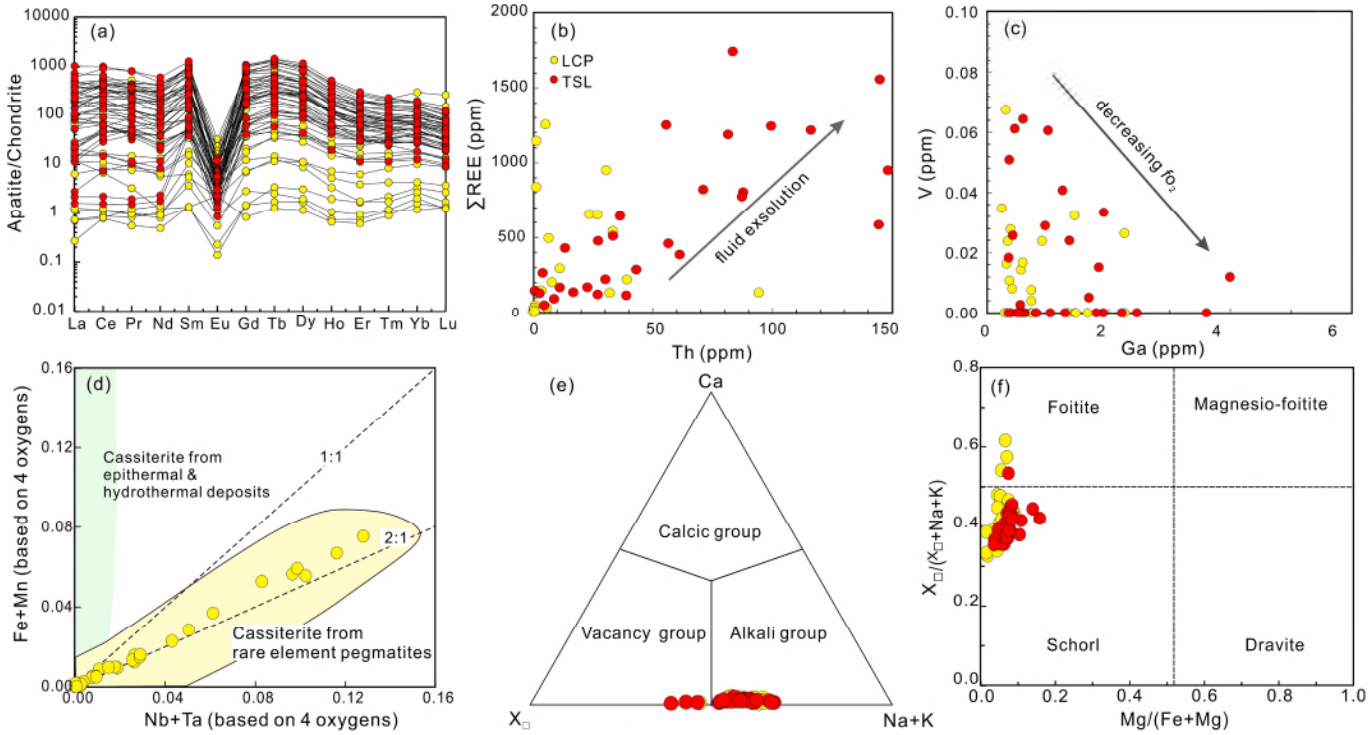

Fig. 4. Geochemical compositions of accessory minerals in the FJS leucogranites. (a) Chondrite-normalized REE patterns of apatite. Normalizing values are from Sun and McDonough (1989). Plots of (b) REEs versus Th and (c) V versus Ga for apatite. (d) Bivariate plots of selected trace elements in cassiterite (according to Tindle and Breaks, 1998). (e–f) Chemical composition of tourmaline.

secondary muscovite (PM and SM) based on texture and chemistry. The PM is coarse-grained and euhedral–subhedral with similar sizes to other rock-forming minerals (Fig. 2). In contrast, the SM is mostly fine-grained, interstitial, or part of the coarse-grained PM, which has been altered (Fig. 2). Some coarse-grained muscovite in the granites plots as SM in a Ti–Mg–Na ternary plot (Fig. 3a). This may be due to: (1) the evolved magmas parental to the muscovite granites having relatively low Ti, Na, Mg contents; or (2) hydrothermal alteration by magmatic fluids during the late stages of magmatic evolution (Zhang et al., 2017c).

4.1.2. Feldspar

Plagioclase occurs as tabular subhedral–anhedral crystals with polysynthetic twinning and continuous compositional zoning. The composition of plagioclase ranges from $Ab_{99.7}An_0Or_{0.2}$ to $Ab_{97.9}An_{0.9}Or_{1.2}$. Alkali feldspar occurs as large grains of orthoclase, grains of cross-hatched microcline, and intergranular grains of perthite, with compositions ranging from $Ab_{3.5}An_{1.9}Or_{94.6}$ to $Ab_{1.9}An_{11.1}Or_{86.9}$ (Figs. 2 and 3b).

4.1.3. Apatite

Representative BSE images of apatite from the leucogranites show that most grains are prismatic or subhedral (Fig. 5 and S1) and enclosed by rock-forming minerals (mainly plagioclase) (Fig. S1), which indicates the apatite is of magmatic origin (Harlov, 2015). Some grains exhibit a patchy texture, with bright zones and micro-pores or fractures, indicative of post-crystallization hydrothermal activity (Harlov and Förster, 2003). Contents of CaO (47.5–56.5 wt%) and P_2O_5 (40.0–44.4 wt%) are consistent with the stoichiometric composition of apatite. Apatite grains

have high F (>3.05 wt%) and low Cl contents (<0.27 wt%) contents. The high F/Cl ratios (>200) indicate that the apatite has been affected by hydrothermal processes, which can leach Cl and lead to high F/Cl ratios (Webster and Piccoli, 2015; Zhang et al., 2020).

The trace elements Na, Fe, Ti, Pb, rare earth elements (REE), Sc, Sr, U, and Th were detected in apatite, whereas Al, K, V, Cr, Cu, Zn, Ge, Zr and Nb were generally below detection limits (Supplementary Table 3). In the Chondrite-normalized REE diagram (Fig. 4a), all apatite grains have nearly flat REE patterns with enrichment in middle REE (MREE; Sm to Dy), which is a feature of magmatic apatite (Webster and Piccoli, 2015) and typical of apatite from S-type or highly fractionated I-type granites in the Lachlan Fold Belt of southeastern Australia (Sha and Chappell, 1999). The ΣREE contents of apatite grains from the TSL granites (49.9–1743 ppm) are higher than those from the LCP granites (2.85–1255 ppm) (Fig. 4a). The apatite has low and variable LREE/HREE ratios (0.06–10.9; mostly < 2) and large negative Eu anomalies (Eu/Eu* = 0.003–0.11). These features are consistent with the effects of hydrothermal fluids (Zhang et al., 2020, 2021a,b).

4.1.4. Cassiterite

Cassiterite grains from a representative W–Sn-mineralized leucogranite sample were analyzed for trace elements (Fig. S2). They are characterized by low contents of high-field-strength elements (HFSE; e.g., Zr, Hf, Nb and Ta). Iron, W, and Ti contents are high in all cassiterite grains. Iron contents range from 219 to 10864 ppm, and W from 3.75 to 1870 ppm, and Ti from 65.6 to 2047 ppm. Uranium, Sc, and Al are present in small amounts in cassiterite, with U from 0.15 to 1752 ppm and Sc = 1.9–124 ppm.

4.1.5. Tourmaline

Tourmaline exhibits moderate variations in contents of FeO (14.0–16.1 wt%), MgO (0.12–1.51 wt%), and Al_2O_3 (32.9–35.3 wt%), and relatively small variations in contents of minor elements, such as Na_2O (1.16–1.93 wt%), CaO (0.03–0.15 wt%), TiO_2 (0.06–0.63 wt%), and F (0.21–0.82 wt%). All tourmaline has negligible Cl contents (<0.01 wt%). Based on the nomenclature of Henry et al. (2011), most of tourmalines belong to the alkali group, with variable Ca contents and X-site vacancies (Fig. 4e). They have compositions corresponding to the X-vacancy type, with (Na + K) < 0.7 atoms per formula unit (apfu), $^{X}\square$ > 0.5 apfu, and Ca < 0.03 apfu (Supplementary Table 3). In a $^{X}\square/(^{X}\square$ + Na + K) versus Mg/(Fe + Mg) diagram (Fig. 4f), they plot mainly in the schorlitic field.

Most of the trace element contents are < 10 ppm. Relatively high contents (several to hundreds of ppm) were determined for Li, Be, Sc, V, Zn, Ga, Sr, and Sn, whereas very low contents, locally below detection limits, were determined for Cu, Rb, Cs, Zr, Hf, W, Bi, Th, and U. Tourmaline has ΣREE contents of 0.30–8.11 ppm.

4.2. In situ dating of accessory minerals

4.2.1. Zircon U–Pb dating

Zircon grains from a leucogranite sample (LCP04) have variable Th (38–614 ppm) and U (158–1212 ppm) contents, with Th/U ratios of 0.08–0.61. Fifteen analyses were concordant and yielded a weighted-mean age of 811.6 ± 5.8 Ma (MSWD = 0.25) (Figs. 5a and b), that is interpreted as the crystallization age of the FJS leucogranite. Moreover, four analyses yielded younger $^{206}Pb/^{238}U$ ages of 787–667 Ma (Fig. 5a), which might be due to Pb loss.

4.2.2. Cassiterite and apatite U–Pb dating

The U–Pb ages were calculated by a linear regression in Tera–Wasserburg diagrams (Tera and Wasserburg, 1975) because apatite and cassiterite incorporate common Pb. All U–Pb dating results are defined as the lower intercept with the Concordia, as determined by

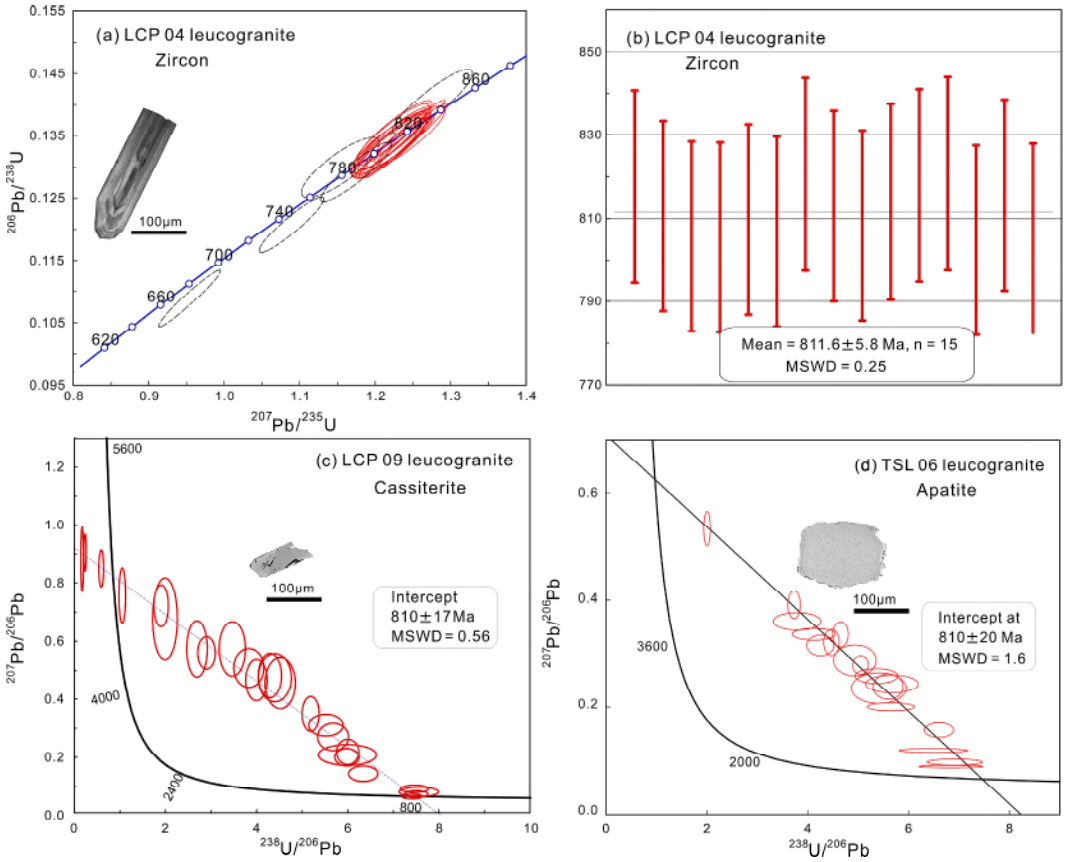

Fig. 5. In situ U–Pb ages of accessory minerals from the representative samples of FJS leucogranites. (a) SIMS U–Pb Concordia diagram for zircon; (b) SIMS U–Pb weighted-mean ages of zircon; (c) LA–ICP–MS U–Pb dating of the cassiterite. (d) LA–ICP–MS U–Pb dating of the apatite.

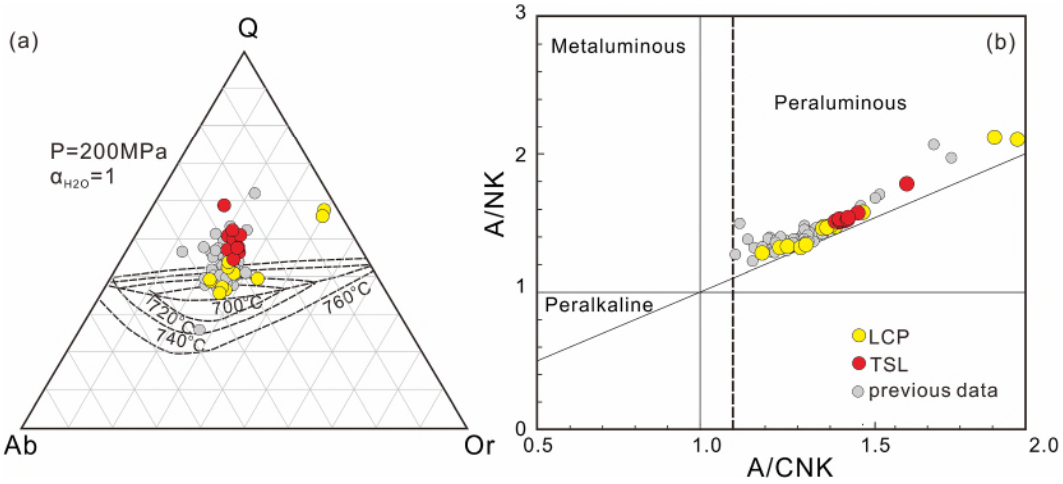

Fig. 6. Plots of (a) Q–Ab–Or and (b) A/NK (molar $Al_2O_3/[Na_2O + K_2O]$) vs A/CNK (molar $Al_2O_3/[CaO + Na_2O + K_2O]$) for representative samples in the FJS district.

linear regression of discordant arrays. The U–Pb isotopic data and Tera-Wasserburg diagrams are presented in Supplementary Table 3 and shown in Fig. 5, respectively.

Twenty-six analyses were conducted on 26 cassiterite grains from sample LCP09. They yielded variable U contents (2.74–392 ppm) and yield a concordia lower intercept age of 810 ± 17 Ma (MSWD = 0.56, n = 26) (Fig. 5c), that is interpreted as the crystallization age of cassiterite in the FJS leucogranite. An in-house cassiterite standard (KA) from the Baiganhu W–Sn ore deposit was used for quality control and yielded a lower intercept age of 406 ± 15 Ma (MSWD = 1.16, n = 5), which is within error of the age reported by Tang et al. (2020).

The U–Pb age for apatite from sample TSL06-06, as determined using the lower intercept, is 810 ± 20 Ma (MSWD = 1.6, n = 18) (Fig. 5d), which is within error of the zircon age, implying the apatite grains from the FJS leucogranite crystallized at *ca.* 810 Ma. The U–Pb isotopic data for apatite from sample LCP09 define a regression line that yields a well-defined lower intercept age of 782 ± 23 Ma (MSWD = 0.72, n = 16) (Fig. S3). This age is slightly younger than the zircon age, possibly due to late-stage hydrothermal processes, which is indicated by the texture and composition of the apatite. The in-house Qinghu apatite standard was used for data quality control and yielded a lower intercept age of 158.5 ± 4.1 Ma (MSWD = 1.6, n = 9), which is within error of the reported age of 159.5 ± 0.2 Ma (Li et al., 2013).

4.3. *Whole-rock major and trace elements and Nd isotopes*

The FJS leucogranites have high SiO_2 contents (72.4–79.0 wt%), low CaO (0.06–0.48 wt%), TiO_2 (0.01–0.04 wt%), MgO (0.02–0.56 wt%), P_2O_5 (0.19–0.37.wt%), and MnO (0.04–0.10 wt%) contents, and variable Na_2O (0.32–4.18.wt%), Fe_2O_{3T} (0.88–1.97 wt%), and K_2O (2.47–5.97 wt%) contents. In a quartz (Q)–albite (Ab)–orthoclase (Or) ternary plot, the samples plot in the eutectic field (Fig. 6a). In a molar $Al_2O_3/(CaO + Na_2O + K_2O)$ versus $Al_2O_3/(Na_2O + K_2O)$ (A/CNK versus A/NK) diagram, all samples plot in the peraluminous field (Fig. 6b).

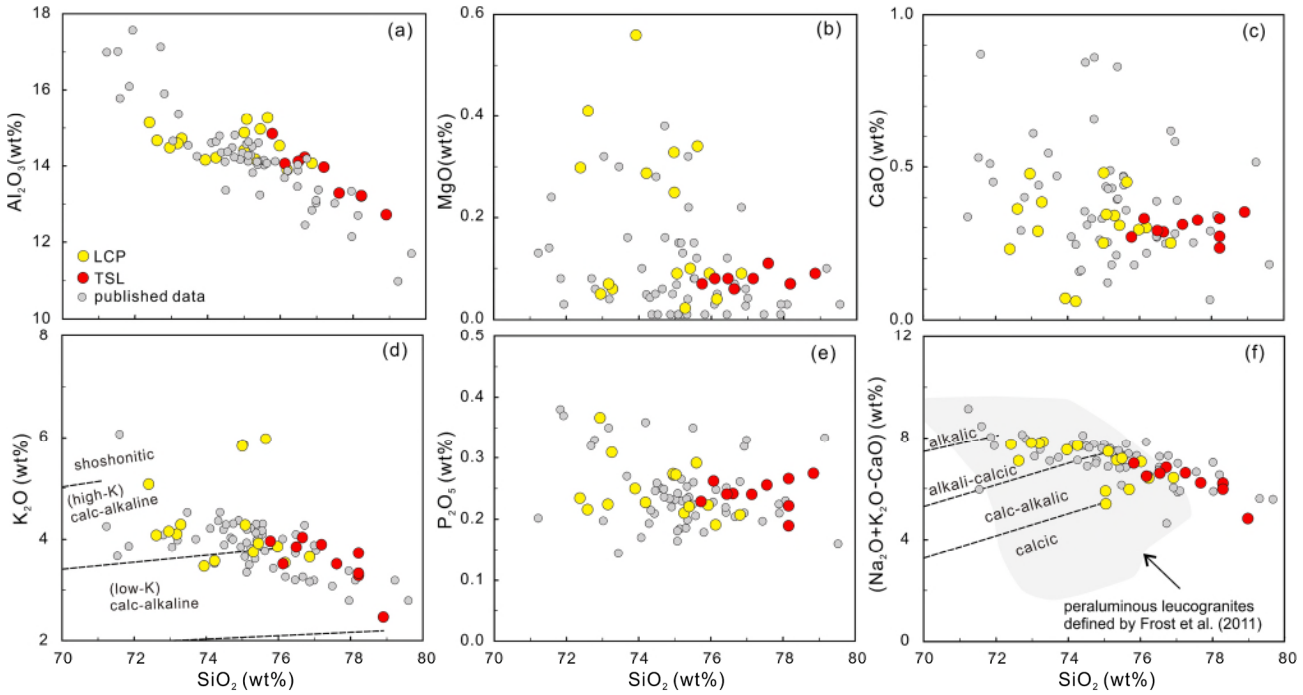

Fig. 7. Harker diagrams for representative samples of the FJS leucogranites. K_2O versus SiO_2 (after Peccerillo and Taylor, 1976). ($Na_2O + K_2O - CaO$) versus SiO_2 (after Frost et al., 2001).

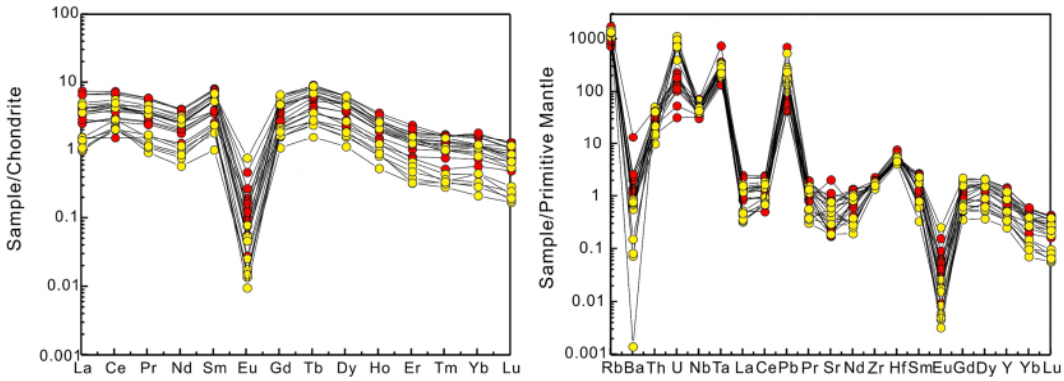

Fig. 8. (a) Chondrite-normalized REE patterns and (b) Primitive mantle-normalized trace element diagrams for the FJS leucogranites. Normalizing values are taken from Sun and McDonough (1989).

They have high total alkali contents of 5.18–8.29 wt% and plot as calc-alkaline rocks in a K_2O versus SiO_2 diagram (Fig. 7). On Harker diagrams, most of the major elements define linear trends (Fig. 7).

The FJS leucogranites have extremely low ΣREE contents of 2.71–13.6 ppm. They are characterized by highly fractionated "V-shaped" REE patterns ($[La/Yb]_N$ = 1.70–7.23) with large negative Eu anomalies (δEu = 0.01–0.09) (Fig. 8a). The FJS leucogranites exhibit a clear tetrad effect ($TE_{1,3}$) (Fig. 9). On a primitive mantle-normalized trace element diagram, all samples exhibit strong enrichments in Rb, Th, U, and K, and depletion in Ba, Sr, P, Ti, and Nb (Fig. 8b). They have variably high Rb/Sr (13.2–202) and low Nb/Ta (2.12–4.06) and Zr/Hf (10.8–3.5) ratios (Fig. 10). Whole-rock zircon saturation temperatures, calculated using the method of Waston and Harrison (1983) are 640–670 °C.

The samples have variable $^{143}Nb/^{144}Nb$ ratios (0.513226–0.513363), corresponding to negative $\varepsilon_{Nd}(t)$ values (−6.6 to − 7.6), with two-stage Nd model ages of 2.02–2.10 Ga.

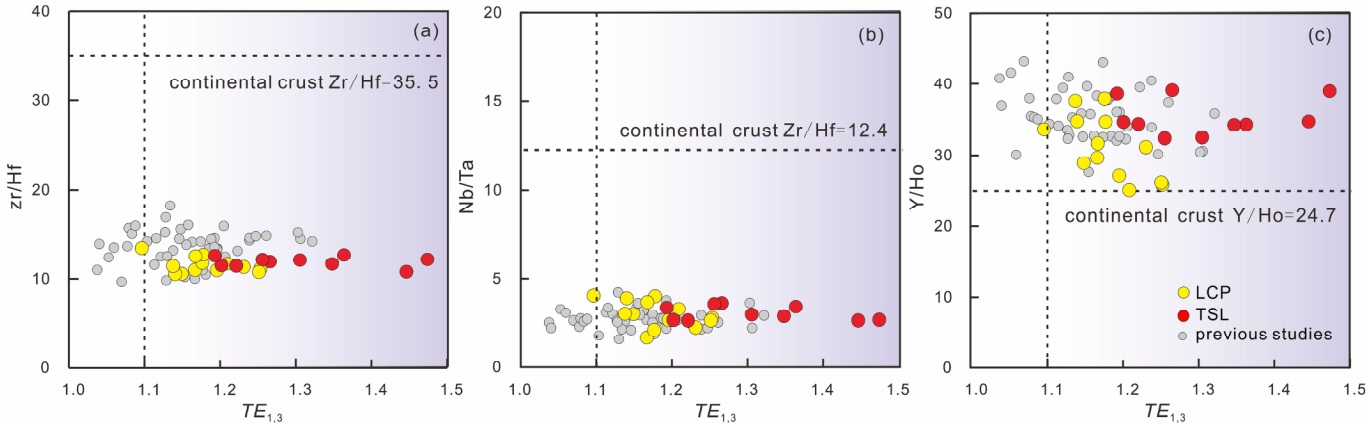

Fig. 9. Plots of the tetrad effect ($TE_{1,3}$) versus (a) Zr/Hf, (b) Nb/Ta, and (c) Y/Ho (after Irber, 1999). The dotted line defines the field of clearly visible tetrad effects ($TE_{1,3}$ = 1.10).

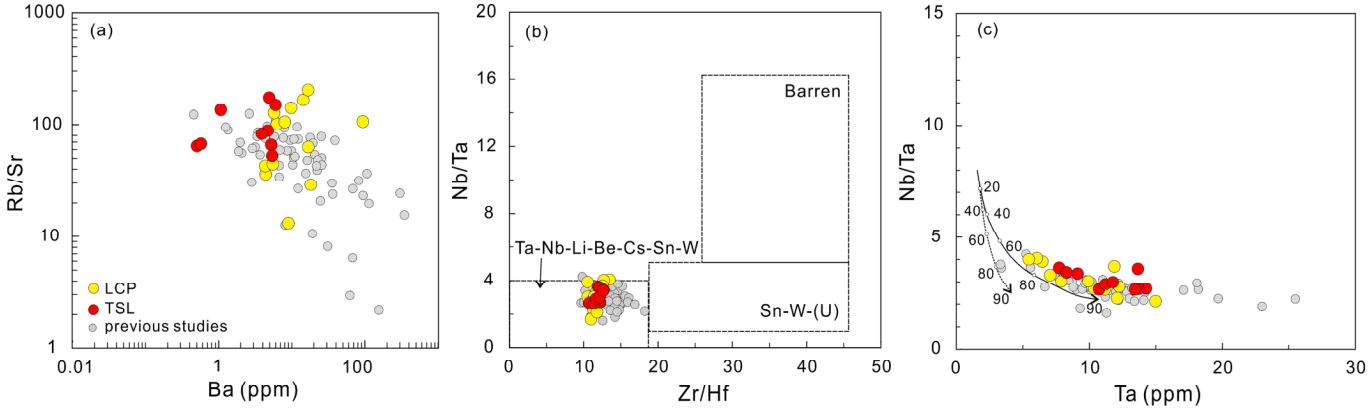

Fig. 10. Elemental variations of the Neoproterozoic leucogranites from the FJS region. Plots of (a) Rb/Sr versus Ba diagram and (b) whole rock Zr/Hf versus Nb/Ta (after Ballouard et al., 2016). (c) Plots showing fractional crystallization of Bt_{10} + Ms_{10} + Qz/Pl_{80} (solid line) and Bt_{10} + Ms_{10} + $Qz/Pl_{79.5}$ + $Ilm_{0.5}$ (dashed line). Initial compositions and partition coefficients used in the calculation are from Ballouard et al. (2016). Numbers accompanying the lines represent the degree of fractionation.

5. Discussion

5.1. Petrogenesis of the FJS leucogranites

The Neoproterozoic leucogranites in the FJS region are calc-alkaline rocks with high SiO_2 contents. They have strongly peraluminous compositions (Fig. 6b) and minerals (e.g., primary muscovite and monazite) that are typical of S-type granites, implying the source was metasedimentary rocks (Chappell and White, 2001). The calculated zircon saturation temperatures provide an estimate of the magma temperature. The presence of inherited zircons means the calculated temperatures (640–670 °C) represent the maximum temperature of partial melting (Miller et al., 2003). Metasedimentary rocks that have never experienced a previous episode of melting tend to yield partial melts at low temperatures (Annen and Sparks, 2002). Some field and petrographic evidence precludes the possibility of mixing with mantle-derived or other crustal melts, including the lack of mafic enclaves, relatively low (Fe_2O_{3T} + MgO) contents, and low Mg# values of most samples (<20) (Martin et al., 2005; Champion and Bultitude, 2013). In addition, the increasing Rb/Sr ratios with decreasing Sr and Ba contents (Fig. 10), as well as negative Eu anomalies (Fig. 8), imply that the leucogranites were derived by melting that consumed muscovite (i.e., muscovite dehydration melting; Inger and Harris, 1993; Gao and Zeng, 2014; Weinberg and Hasalová, 2015). The leucogranites have negative $\varepsilon_{Nd}(t)$ values of − 7.6 to − 6.6, with two-stage Nd model ages of *ca.* 2.0 Ga. Therefore, it is reasonable to deduce that the parental magmas of the FJS leucogranites were the product of muscovite dehydration melting of basement rocks older than *ca.* 2.0 Ga.

Although all the samples have broadly similar geochemical compositions, the geochemical diversity of the leucogranites might reflect variable degree of partial melting and/or fractional crystallization of the parental melts. The FJS leucogranites consist mainly of quartz and feldspar, and their CIPW normative compositions are located at the eutectic point of the granite system in the Q–Ab–Or diagram (Fig. 6a; Johannes and Holtz, 1996), suggesting that the parental magmas underwent extensive fractional crystallization. The linear variations on Harker diagrams also show that the parental melts of the FJS leucogranites underwent significant fractionation (Fig. 7). In general, with increasing silica content, Al_2O_3, MgO, CaO, and K_2O contents decrease, whereas Na_2O increases, and TiO_2, Fe_2O_{3T} and P_2O_5 show no clear trends (Fig. 7). The granitic rocks are characterized by low TiO_2, CaO and MgO contents, and negative Ba, Sr, Eu, and Nb anomalies in multi-element diagrams (Fig. 8). The depletion in Ti is consistent with the fractionation of Ti-bearing phases (e.g., ilmenite). Fractionation of plagioclase and K-feldspar from melts can lead to negative Eu, Sr, and Ba anomalies (Hanson, 1978; Healy et al., 2004; Deschamps et al., 2018). Given that the LREE contents of granites are predominantly buffered by accessory minerals (e.g., apatite, allanite, and monazite) (Miller and Mittlefehldt, 1982; Ayres and Harris, 1997), it is likely that the extremely low contents of LREE in the FJS leucogranites are due to strong fractionation. Variable degree of partial melting would result in variations in ratios of 'fanning' style of the LREE in the normalized diagram (Deschamps et al., 2018), which is not the case for the studied samples.

Boron is a volatile element, and is strongly fractionated into late-stage melts and associated hydrothermal fluids. Experimental studies suggest that B plays an important role in the evolution of magmatic systems (Thomas, 2002; Thomas et al., 2003). It acts as a fluxing agent for granitic melts, enabling them to remain liquid to lower temperatures and allowing a greater degree of fractional crystallization (London, 1987; Dingwell et al., 1996), and decreases the melt viscosity at low water concentrations (<4 mol.%) (Bartels et al., 2013). Tourmaline is prevalent in the FJS leucogranites and coexists with quartz and plagioclase (Zhao et al., 2021b). Leucocratic peraluminous magmas that are saturated with respect to tourmaline may contain several wt.% B_2O_3 in the melt (Dingwell et al., 1996). Therefore, the high B content had an important role in the magmatic evolution of the FJS leucogranites, lowering the solidus temperature and viscosity, and enhancing the degree of fractional crystallization.

Niobium and Ta have a similar charge and ionic radius and remain largely immobile during magmatic differentiation (Dostal and Chatterjee, 2000; Shellnutt et al., 2009). The FJS leucogranites have low Nb/Ta ratios (1.71–4.06) and high Ta contents (5.45–30.2 ppm). Although low Nb/Ta ratios could be a result of residual biotite during low-*T* partial melting (Xiong et al., 2011), high Ta contents are rare in silicic melts (Stepanov et al., 2014). Decreasing Nb/Ta ratios could be produced by fractionation of mica and Ti-bearing minerals (Linnen and Keppler, 1997; Stepanov et al., 2014). However, even more than 90 % fractional crystallization of muscovite + biotite + plagioclase + quartz cannot produce Ta-rich melts chemically similar to the FJS leucogranites (Fig. 10c). Therefore, the low Nb/Ta ratios are more likely the result of hydrothermal alteration (Ballouard et al., 2016). Some elemental ratios are sensitive to magmatic–hydrothermal interactions, such as the Zr/Hf (26–46) and K/Rb (200–300) ratios of silicate melts, which are higher than those of aqueous fluids (Zr/Hf < 26, K/Rb < 150) (Bau, 1996; Irber, 1999). The FJS leucogranites have much lower Zr/Hf (11–14) and K/Rb (28–67) ratios than silicate melts, being similar to those of aqueous fluids, and consistent with magmatic–hydrothermal interactions. The presence of quartz veins in the thin sections (Fig. S4), and the compositions of apatite also provide strong evidence for late hydrothermal processes. Therefore, the parental magmas of the FJS leucogranites experienced protracted differentiation and intense fluid–melt interaction.

As such, we propose that the Neoproterozoic muscovite-tourmaline leucogranites are highly fractionated S-type granites. Their parental magmas were formed by partial melting of ancient crustal materials dominated by pelites, followed by prolonged differentiation and late-stage hydrothermal processes.

5.2. Relationship between FJS leucogranite and W–Sn mineralization: Evidence from accessory minerals

Physico-chemical processes and magmatic–hydrothermal evolution play important roles in granite-related W–Sn mineralization. The mineralogical and geochemical fingerprints can be recorded by minerals (Ulrich et al., 2002; Audétat and Pettke, 2003). Apatite [$Ca_5(PO_4)_3$(OH, F, Cl)] is a ubiquitous accessory mineral in W–Sn bearing granites and crystallizes from the early magmatic to late hydrothermal stages (Bouzari et al., 2016; Hoskin et al., 2000). Therefore, it can be an effective tracer of both magmatic and hydrothermal processes (Harlov, 2015; Harlov et al., 2005; Qu et al., 2022; Wang et al., 2014; Webster and Piccoli, 2015). The chemical composition of apatite can be modified by late hydrothermal fluids (Zeng et al., 2016; Cao et al., 2019), characterized by the leaching of trace elements, such as S, REE, Th, V, and Ga (Harlov and Förster, 2003; Harlov et al., 2005; Li and Zhou, 2015). The tetrad REE patterns of apatite grains from the leucogranites (Fig. 4a) are indicative of intensive mineral–fluid interactions (Bau, 1996; Irber, 1999). The LCP apatite grains have lower REE contents and more obvious tetrad patterns (especially the HREE) than those from the TSL, which indicate relatively intense post-crystallization hydrothermal activity in the LCP leucogranites and might also explain the younger age of LCP apatite (Fig. S3; Zhang et al., 2020, 2021b). Fluid exsolution can increase the partition coefficients for REE and Th, leading to higher contents of these elements in magmatic–hydrothermal apatite (Watson and Green, 1981; Prowatke and Klemme, 2006; Qu et al., 2021). The apatite from the FJS leucogranites has elevated REE and Th contents (Fig. 4b) and low SO_3 contents (<0.015 wt% and mostly lower than the detection limit; Supplementary Table 3), indicative of fluid exsolution. Moreover, REE can form strong complexes with chloride ions (Migdisov et al., 2009), which enhance the transportation and mobility of REE (van Dongen et al., 2010). The stability of LREE–chloride complexes is higher than that of HREE–chloride complexes at elevated temperatures

(Williams-Jones et al., 2012). Gallium and V in apatite can be used to estimate the oxidation state of magma, and a lower oxidation state increases Ga content and decreases V content in apatite (Pan et al., 2016; Qu et al., 2021). The negative correlation between the Ga and V contents of apatite (Fig. 4c) in the FJS leucogranite provides further support the decreasing oxygen fugacity during magmatic evolution.

The chemical composition of tourmaline is controlled by a range of factors including host rock lithology, coexisting minerals, fluid composition, and P–T–f_{O2} conditions, and is widely used as a proxy of magmatic–hydrothermal processes related to W–Sn ore deposits (London and Manning, 1995; Dutrow and Henry, 2011, 2016; Slack and Trumbull, 2011; Harlaux et al., 2020, 2021; Guo et al., 2022). In the FJS leucogranites, disseminated tourmaline is interstitial to quartz, feldspar, and muscovite, and is texturally homogeneous, indicating late crystallization. Most of the tourmaline grains have relatively uniform chemical compositions with Fe/(Fe + Mg) = 0.86–0.99 and Na/(Na + Ca) = 0.95–0.99, thereby belonging to the schorl series (Fig. 4f). The enrichments in Fe and Al (Fe = 2.00–2.31 apfu, and Al = 6.75–7.01 apfu) are consistent with the strongly peraluminous whole-rock compositions of the host granites (A/CNK $\geq$ 1.1 and high $FeO_T/[FeO_T + MgO]$ = 0.41–0.91). Such textural and chemical characteristics are consistent with a primary magmatic origin (London and Manning, 1995; Drivenes et al., 2015; Guo et al., 2022). Some of tourmaline grains plot in the foitite field (Fig. 4f). The chemical evolution toward a foititic composition with elevated $^{X}\square$ in magmatic to hydrothermal tourmaline has been documented in many granite–pegmatite systems worldwide (London and Manning, 1995; Trumbull and Chaussidon, 1999), indicating an increase in fluid–rock interactions during the period of tourmaline nucleation and growth. The late magmatic tourmaline has low $Fe^{3+}/(Fe^{3+}+ Fe^{2+})$ ratios (0.04–0.21), suggesting it precipitated from a reduced peraluminous granitic magma, in which Sn was dominantly Sn^{2+} rather than Sn^{4+}, thereby favoring Sn enrichment in the residual silicate melt during magmatic differentiation (Linnen et al., 1996). The high contents of incompatible elements (e.g., Li, Nb, Ga, and Sc) are similar to those of late magmatic tourmaline in other highly fractionated Sn-bearing granites (Drivenes et al., 2015; Guo et al., 2022). The crystallization of late magmatic tourmaline consumes a large amount of B in the melt, leading to a marked decrease in water solubility and enhanced fluid exsolution (Pichavant, 1981, 1987; Holtz et al., 1993).

The composition of cassiterite records its precipitation environment and mineralization type (Möller et al., 1988; Murciego et al., 1997). Tungsten enrichment in cassiterite from granite-related deposits, either in the cassiterite lattice or as mineral/fluid inclusions hosted in cassiterite, can be attributed to highly fractionated granitic magmas that are generally enriched in W, Nb, Ta, and Zr (Guo et al., 2018). The Fe–W–Nb–Ta-rich nature of the cassiterite grains of the present study indicates that incorporation of Fe might follow the coupled substitution $Fe^{2+}+ 2(Nb, Ta)^{5+} = 3(Sn, Ti)^{4+}$ and $Fe^{3+} + (Nb, Ta)^{5+} = 2(Sn, Ti)^{4+}$ (Izoret et al., 1985; Möller et al., 1988). This substitution also corresponds to that of cassiterite in the plot of Fe + Mn versus Nb + Ta proposed by Tindle and Breaks (1998), indicating a high-temperature system (i.e., rare-metal granites, pegmatites and greisens). The Sn contents of the FJS leucogranites are 53–249 ppm (Xiang et al., 2020), which are much higher than those of the average continental crust (1.5–2.5 ppm; Rudnick and Gao, 2003). During partial melting of ancient crustal rocks in the FJS, Sn was concentrated in the reduced silicic magmas, because Sn^{2+} is an incompatible element (Sui et al., 2020; Liu et al., 2022). Tin was further enriched in the residual magmas and hydrothermal fluids during magma ascent and emplacement. The occurrence of cassiterite in the FJS leucogranite reflects Sn enrichment in the magma. Moreover, the cassiterite U–Pb age (*ca.* 810 Ma) is consistent with the zircon U–Pb age (*ca.* 812 Ma). As such, there was a close temporal and genetic link between granitic magmatism and W–Sn polymetallic mineralization.

These mineral constraints and the presence of quartz veins and ore minerals (e.g., cassiterite and scheelite) provide strong evidence for magmatic–hydrothermal processes and ore metal mineralization in the FJS district. Therefore, the FJS Neoproterozoic W–Sn mineralization was the result of extensive magmatic differentiation under relatively reducing conditions, followed by magmatic–hydrothermal processes in the ore-hosting granites. Neoproterozoic S-type granitoids were widely developed during the Jiangnan Orogeny (Wu et al., 2006; Zheng et al., 2007; Zhao et al., 2011; Wang et al., 2014; Li et al., 2021), but only rare granitic intrusions host economic W–Sn deposits. Unusually, the FJS leucogranite contain W–Sn–(Ta–Nb) mineralization (Xia, 1985; Xiang et al., 2020; Lv et al., 2021). Therefore, the mineralogical and geochemical characteristics of the FJS leucogranites can be used to evaluate the W–Sn–(Ta–Nb) ore-forming potential of other Neoproterozoic S-type granites.

5.3. Implications for magmatism in the western Jiangnan Orogen

The Neoproterozoic Jiangnan Orogen had a complex tectonic evolution during the Precambrian and played an important role in the evolution of Rodinia (Shu et al., 2019; Wang et al., 2004, 2016; Zheng et al., 2019). Previous studies on the magmatism, stratigraphy, and mineralization in the Jiangnan Orogen have revealed the processes that formed the orogen (Huang et al., 2023; Kou et al., 2021; Li et al., 2021; Wan et al., 2021; Wang et al., 2017, 2019, Zhang et al., 2019, 2023; Zhou et al., 2009). However, compared with the comprehensive studies of the eastern Jiangnan Orogen, western areas have received little attention.

Most of the Neoproterozoic granitoids in the western Jiangnan Orogen have an S-type affinity, with high SiO_2 contents and A/CNK values, and were sourced from ancient continental crust without significant juvenile magmatic input (Li et al., 2003; Zhao et al., 2013; Chen et al., 2018; Wei et al., 2018; Shu et al., 2021). Their mineralogical and geochemical features are similar to those of muscovite-bearing peraluminous granitoids (MPGs) that are common in orogenic belts, and generally form from the thickened crust (Barbarin, 1990, 1996; Inger and Harris, 1993). However, previous studies have different views on the geochronology framework and tectonic setting of granitoids in the western Jiangnan Orogen. Previous studies have suggested emplacement ages of 835–820 Ma (Yao et al., 2019); however, it has also been proposed that the Neoproterozoic felsic magmatism had main age peaks at *ca.* 812 Ma (Wan et al., 2021). Other studies have proposed that the peraluminous plutons formed during the amalgamation of the Yangtze and Cathaysia blocks (i.e., during the *syn*-orogenic stage), because the coeval mafic rocks have ages of 850–830 Ma (Zhou et al., 2004). It has also been suggested that the granitic plutons formed during the post-orogenic stage (Wang et al., 2013, 2014b; Zhang et al., 2013; Yan et al., 2019), and that the Neoproterozoic mafic and silicic intrusions in the western Jiangnan Orogen range in age from 906 Ma to 820 Ma (Wan et al., 2021).

The Neoproterozoic sedimentary rocks (i.e., the FJS Group and its equivalents) are considered to have been deposited prior to the felsic magmatism (Wang et al., 2007; Zhao et al., 2011). Previous zircon U–Pb dating results reveal their depositional age from 870 Ma to 830 Ma (Zhao and Cawood, 2012), which also constrains the maximum deposition age, as well as the subsequent felsic intrusions. Granitic plutons in the western segment (including the FJS, Sanfang, Bendong and Yuanbaoshan areas) crystallized during 839–804 Ma (Li et al., 1999; Wang et al., 2011a,b; Yan et al., 2021; Shu et al., 2021 and references therein). Here, through our detailed geochronological study, the in-situ zircon age result is *ca.* 812 Ma, which represents the emplacement age of the FJS leucogranites. Combined with other high-precision dating and geochemical data, it suggests that orogenesis continued until at least *ca.* 812 Ma (Yao et al., 2013; Zhao, 2015).

Tectonic–magmatic–sedimentary studies have shown that the Jiangnan Orogen was formed by a Neoproterozoic orogenic event. Continent–continent collision generated peraluminous S-type granites in the syn- or post-collisional stage of an orogenic cycle (Shu et al., 2019). We

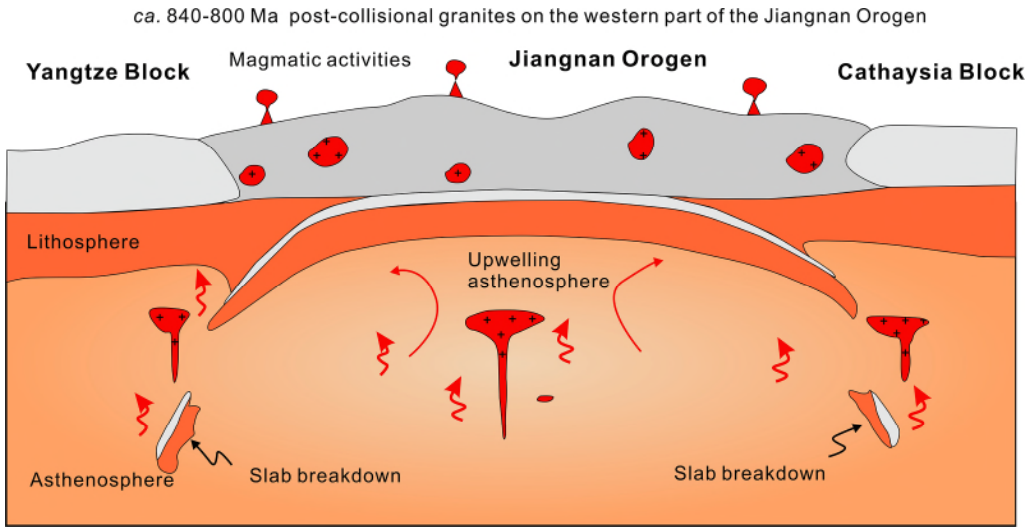

Fig. 11. Schematic model of the Neoproterozoic evolution of the Jiangnan Orogen (modified after Wan et al., 2021).

infer that the 840–800 Ma S-type granites in the western Jiangnan region, represent the final stage of the Jiangnan Orogeny (Fig. 11).

6. Conclusions

(1) A representative sample of the FJS leucogranites yields a zircon U–Pb age of 811.6 ± 5.8 Ma. Apatite U–Pb isotope data yield a lower intercept age of 810 ± 20 Ma, which is consistent with the zircon age. Cassiterite U–Pb dating yields a concordia lower intercept age of 810 ± 17 Ma, which is consistent with the emplacement age of the pluton. We suggest a close temporal link between granitic magmatism and W–Sn mineralization.

(2) The parental magmas of the FJS leucogranites were derived by melting of Paleoproterozoic pelitic rocks, which then experienced extensive fractional crystallization. Geochemical compositions of accessory minerals (apatite, tourmaline, and cassiterite), combined with the dating results, indicate the W–Sn mineralization in the FJS region was formed in a granite-related, magmatic–hydrothermal system controlled by the FJS leucogranites.

(3) We suggest the FJS leucogranites formed in a post-orogenic extensional setting. The nature of these and other granites (*ca.* 840–800 Ma) in the western segment of Jiangnan Orogen, indicates the granites produced by crustal remelting record the last stage of the Jiangnan Orogeny.

CRediT authorship contribution statement

Xiao-Yan Jiang: Investigation, Methodology, Data curation, Writing – original draft, Formal analysis, Project administration, Funding acquisition, Visualization. **Jia Guo:** Investigation, Formal analysis, Visualization. **Wei-Guang Zhu:** Conceptualization, Investigation, Supervision, Resources. **Jin-Cheng Luo:** Data curation, Formal analysis, Funding acquisition. **Ke-Nan Jiang:** Data curation.

Declaration of competing interest

The authors declare that they have no known competing financial interests or personal relationships that could have appeared to influence the work reported in this paper.

Data availability

Data will be made available on request.

Acknowledgements

We thank Yan-Wen Tang, Jun-Jie Han for assistance in LA–ICP–MS analyses, and Xiang Li, Yun Li, Wen-Qing Zheng for help during the EPMA work. This work was supported by the Guizhou Provincial Science and Technology Projects (No. ZK[2021] 207, No. ZK[2023] 052 and No. [2018]1423), and a special fund managed by the State Key Laboratory of Ore Deposit Geochemistry.

Appendix A. Supplementary material

Supplementary data to this article can be found online at https://doi.org/10.1016/j.precamres.2024.107301.

References

Andersson, S.S., Wagner, T., Jonsson, E., Fusswinkel, T., Whitehouse, M.J., 2019. Apatite as a tracer of the source, chemistry and evolution of ore-forming fluids: The case of the Olserum-Djupedal REE-phosphate mineralisation, SE Sweden. Geochim. Cosmochim. Acta 255, 163–187.
Annen, C., Sparks, R.S.J., 2002. Effects of repetitive emplacement of basaltic intrusions on thermal evolution and melt generation in the crust. Earth Planet. Sci. Lett. 203 (3–4), 937–955.
Audétat, A., Pettke, T., 2003. The magmatic-hydrothermal evolution of two barren granites: A melt and fluid inclusion study of the Rito del Medio and Cañada Pinabete plutons in northern New Mexico (USA). Geochim. Cosmochim. Acta 67, 97–121.
Ayres, M., Harris, N., 1997. REE fractionation and Nd-isotope disequilibriumduring crustal anatexis: constraints from Himalayan leucogranites. Chem. Geol. 139, 249–269.
Ballard, J.R., Palin, J.M., Campbell, I.H., 2002. Relative oxidation states of magmas inferred from Ce (IV)/Ce (III) in zircon: application to porphyry copper deposits of northern Chile. Contributions to Mineralogy and Petrology 144 (3), 347–364.
Ballouard, C., Poujol, M., Boulvais, P., Branquet, Y., Tartese, R., Vigneresse, J.L., 2016. Nb-Ta fractionation in peraluminous granites: A marker of the magmatic-hydrothermal transition. Geology 44 (3), 231–234.
Barbarin, B., 1990. Granitoids: main petrogenetic classifications in relation to origin and tectonic setting. Geolo. J. 25, 227–238.
Barbarin, B., 1996. Genesis of the two main types of peraluminous granitoids. Geology 24 (4), 295–298.
Bartels, A., Behrens, H., Holtz, F., Schmidt, B.C., Fechtelkord, M., Knipping, J., Crede, L., Baasner, A., Pukallus, N., 2013. The effect of fluorine, boron and phosphorus on the viscosity of pegmatite forming melts. Chem. Geol. 346, 184–198.
Bau, M., 1996. Controls on the fractionation of isovalent trace elements in magmatic and aqueous systems: evidence from Y/Ho, Zr/Hf, and lanthanide tetrad effect. Contrib. Mineral. Petrol. 123 (3), 323–333.
Black, L.P., Kamo, S.L., Allen, C.M., Aleinikoff, J.N., Davis, D.W., Korsch, R.J., Foudoulis, C., 2003. TEMORA 1: a new zircon standard for Phanerozoic U-Pb geochronology. Chem. Geol. 200 (1–2), 155–170.
Blevin, P.L., Chappell, B.W., 1995. Chemistry, origin, and evolution of mineralized granites in the Lachlan fold belt, Australia; the metallogeny of I-and S-type granites. Economic Geology 90 (6), 1604–1619.

Bouzari, F., Hart, C.J.R., Bissig, T., Barker, S., 2016. Hydrothermal alteration revealed by apatite luminescence and chemistry: A potential indicator mineral for exploring covered porphyry copper deposits. Econ. Geol. 111, 1397–1410.
Breiter, K., 2012. Nearly contemporaneous evolution of the A-and S-type fractionated granites in the Krušné hory/Erzgebirge Mts. Central Europe. Lithos 151, 105–121.
Cao, M., Evans, N.J., Qin, K., Danišík, M., Li, G., McInnes, B.I.A., 2019. Open apatite Sr isotopic system in low-temperature hydrous regimes: Journal of Geophysical Research. Solid Earth 124, 11192–11203.
Cao, H.W., Pei, Q.M., Santosh, M., Li, G.M., Zhang, L.K., Zhang, X.F., Zhang, Y.H., Zou, H., Dai, Z.W., Lin, B., Tang, L., Yu, X., 2022. Himalayan leucogranites: A review of geochemical and isotopic characteristics, timing of formation, genesis, and rare metal mineralization. Earth Sci. Rev., 104229
Cawood, P.A., Wang, Y.J., Xu, Y.J., Zhao, G.C., 2013. Locating South China in Rodinia and Gondwana: a fragment of Greater Indian Lithosphere? Geology 41 (8), 903–906.
Cawood, P.A., Zhao, G.C., Yao, J.L., Wang, W., Xu, Y.J., Wang, Y.J., 2018. Reconstructing South China in Phanerozoic and Precambrian supercontinents. Earth Sci. Rev. 186, 173–194.
Champion, D.C., Bultitude, R.J., 2013. The geochemical and Sr, Nd isotopic characteristics of Paleozoic fractionated S-types granites of North Queensland: implications for S-type granite petrogenesis. Lithos 162–163, 37–56.
Chappell, B.W., 2004. Towards a unified model for granite genesis. Trans. r. Soc. Edinb. Earth Sci. 95, 1–10.
Chappell, B.W., White, A.J., 2001. Two contrasting granite types: 25 years later. Australian J. Earth Sci. 48 (4), 489–499.
Chen, B., Gu, H., Chen, Y., Sun, K., Chen, W., 2018. Lithium isotope behaviour during partial melting of metapelites from the Jiangnan Orogen, South China: Implications for the origin of REE tetrad effect of F–rich granite and associated rare–metal mineralization. Chem. Geol. 483, 372–384.
Chiaradia, M., Vallance, J., Fontboté, L., Stein, H., Schaltegger, U., Coder, J., Richards, J., Villeneuve, M., Gendall, I., 2009. U-Pb, Re–Os, and 40Ar/39Ar geochronology of the Nambija Au-skarn and Pangui porphyry Cu deposits, Ecuador: implications for the Jurassic metallogenic belt of the Northern Andes. Miner. Depos. 44, 371.
Collins, W.J., 1996. Lachlan Fold Belt granitoids: products of three-component mixing. Earth Environ. Sci. Trans. R. Soc. Edinb. 87 (1–2), 171–181.
Deschamps, F., Duchêne, S., Sigoyer, J., Bosse, V., Benoit, M., Vanderhaeghe, O., 2018. Coeval mantle-derived and crust-derived magmas forming two neighbouring plutons in the Songpan Ganze accretionary orogenicwedge (SWChina). J. Petrol. 58, 2221–2256.
Dingwell, D.B., Hess, K.U., Knoche, R., 1996. Granite and granitic pegmatite melts: volumes and viscosities. Earth Environ. Sci. Trans. r. Soc. Edinburgh 87 (1–2), 65–72.
Dostal, J., Chatterjee, A.K., 2000. Contrasting behaviour of Nb/Ta and Zr/Hf ratios in a peraluminous granitic pluton (Nova Scotia, Canada). Chem. Geol. 163 (1–4), 207–218.
Drivenes, K., Larsen, R.B., Müller, A., Sørensen, B.E., Wiedenbeck, M., Raanes, M.P., 2015. Late-magmatic immiscibility during batholith formation: assessment of B isotopes and trace elements in tourmaline from the Land's End granite, SW England. Contrib. Mineral. Petrol. 169, 1–27.
Dutrow, B.L., Henry, D.J., 2011. Tourmaline: a geologic DVD. Elements 7, 301–306.
Dutrow, B.L., Henry, D.J., 2016. Fibrous tourmaline: a sensitive probe of fluid compositions and petrologic environments. Can. Mineral. 54, 311–335.
Frost, B.R., Barnes, C.G., Collins, W.J., Arculus, R.J., Ellis, D.J., Frost, C.D., 2001. A geochemical classification for granitic rocks. Journal of petrology 42 (11), 2033–2048.
Gao, S., Liu, X., Yuan, H., Hattendorf, B., Günther, D., Chen, L., Hu, S., 2002. Determination of forty two major and trace elements in USGS and NIST SRM glasses by laser ablation-inductively coupled plasma-mass spectrometry. Geostand. Newsl. 26 (2), 181–196.
Gao, L.E., Zeng, L., 2014. Fluxed melting of metapelite and the formation of Miocene high-CaO two-mica granites in the Malashan gneiss dome, southern Tibet. Geochim. Cosmochim. Acta 130, 136–155.
Gao, P., Zheng, Y.F., Zhao, Z.F., 2016. Experimental melts from crustal rocks: a lithochemical constraint on granite petrogenesis. Lithos 266, 133–157.
Garcia-Arias, M., 2020. The never-ending pursuit of a definitive chemical classification system for granites. J. Geosci. 65, 221–227.
Guo, L., Gao, R., 2018. Potential-field evidence for the tectonic boundaries of the central and western Jiangnan belt in South China. Precambr. Res. 309, 45–55.
Guo, J., Zhang, R.Q., Sun, W.D., Ling, M.X., Hu, Y.B., Wu, K., Luo, M., Zhang, L.C., 2018. Genesis of tin-dominant polymetallic deposits in the Dachang district, South China: Insights from cassiterite U-Pb ages and trace element compositions. Ore Geol. Rev. 95, 863–879.
Guo, J., Xiang, L., Zhang, R.Q., Yang, T., Wu, K., Sun, W.D., 2022. Chemical and boron isotopic variations of tourmaline deciphering magmatic-hydrothermal evolution at the Gejiu Sn-polymetallic district, South China. Chem. Geol. 593, 120698.
Hanson, G.N., 1978. The application of trace elements to the petrogenesis of igneous rocks of granitic composition. Earth Planet. Sci. Lett. 38, 26–43.
Harlaux, M., Kouzmanov, K., Gialli, S., Laurent, O., Rielli, A., Dini, A., Chauvet, A., Menzies, A., Kalinaj, M., Fontboté, L., 2020. Tourmaline as a tracer of late-magmatic to hydrothermal fluid evolution: the world-class San Rafael tin(-copper) deposit, Peru. Econ. Geol. 115, 1665–1697.
Harlaux, M., Kouzmanov, K., Gialli, S., Marger, K., Bouvier, A.S., Baumgartner, L.P., Rielli, A., Dini, A., Chauvet, A., Kalinaj, M., Fontboté, L., 2021. Fluid mixing as primary trigger for cassiterite deposition: evidence from in situ δ18O-δ11B analysis of tourmaline from the world-class San Rafael tin (-copper) deposit, Peru. Earth Planet. Sci. Lett. 563, 116889.
Harlov, D.E., 2015. Apatite: A fingerprint for metasomatic processes. Elements 11 (3), 171–176.
Harlov, D.E., Förster, H.J., 2003. Fluid-induced nucleation of (Y+ REE)-phosphate minerals within apatite: Nature and experiment. Part II. Fluorapatite. American Mineralogist 88 (8–9), 1209–1229.
Harlov, D.E., Wirth, R., Förster, H.J., 2005. An experimental study of dissolution-reprecipitation in fluorapatite: Fluid infiltration and the formation of monazite. Contrib. Mineral. Petrol. 150, 268–286.
Harrison, T.M., Watson, E.B., 1984. The behavior of apatite during crustal anatexis: equilibrium and kinetic considerations. Geochim. Cosmochim. Acta 48 (7), 1467–1477.
Healy, B., Collins, W.J., Richards, S.W., 2004. A hybrid origin for Lachlan S-type granites: the Murrumbidgee batholith example. Lithos 79, 197–216.
Hedenquist, J.W., Lowenstern, J.B., 1994. The role of magmas in the formation of hydrothermal ore deposits. Nature 370 (6490), 519–527.
Henry, D.J., Novak, M., Hawthorne, F.C., Ertl, A., Dutrow, B.L., Uher, P., Pezzotta, F., 2011. Nomenclature of the tourmaline-supergroup minerals. Am. Mineral. 96, 895–913.
Holtz, F., Dingwell, D.B., Behrens, H., 1993. Effects of F, B_2O_3 and P_2O_5 on the solubility of water in haplogranite melts compared to natural silicate melts. Contrib. Mineral. Petrol. 113, 492–501.
Hoskin, P.W., Ireland, T.R., 2000. Rare earth element chemistry of zircon and its use as a provenance indicator. Geology 28 (7), 627–630.
Hoskin, P.W.O., Kinny, P.D., Wyborn, D., Chappell, B.W., 2000. Identifying accessory mineral saturation during differentiation in granitoid magmas: An integrated approach. J. Petrol. 41, 1365–1396.
Huang, X., Huang, D., Lu, J., Zhang, R., Ma, D., Jiang, Y., Chen, H., Liu, J., 2023. Neoproterozoic tungsten mineralization: Geology, chronology, and genesis of the Huashandong W deposit in northwestern Jiangxi, South China. Miner. Deposita 58, 771–796.
Inger, S., Harris, N., 1993. Geochemical constraints on leucogranite magmatism in the Langtang Valley, Nepal Himalaya. J. Petrol. 34 (2), 345–368.
Irber, W., 1999. The lanthanide tetrad effect and its correlation with K/Rb, Eu/Eu*, Sr/Eu, Y/Ho, and Zr/Hf of evolving peraluminous granite suites. Geochim. Cosmochim. Acta 63 (3–4), 489–508.
Ishihara, S., 1981. The granitoid series and mineralization.
Izoret, L., Marnier, G., Dusausoy, Y., 1985. Caractérisation cristallochimique de la cassitérite des gisements d'étain et de tungstène de Galice, Espagne. Can. Mineral. 23, 221–231.
Jahn, B.M., Wu, F., Capdevila, R., Martineau, F., Zhao, Z., Wang, Y., 2001. Highly evolved juvenile granites with tetrad REE patterns: the Woduhe and Baerzhe granites from the Great Xing'an Mountains in NE China. Lithos 59 (4), 171–198.
Jiang, X.Y., Li, H., Ding, X., Wu, K., Guo, J., Liu, J.Q., Sun, W.D., 2018. Formation of A-type granites in the Lower Yangtze River Belt: A perspective from apatite geochemistry. Lithos 304, 125–134.
Jiang, S.Y., Radvanec, M., Nakamura, E., Palmer, M., Kobayashi, K., Zhao, H.X., Zhao, K. D., 2008. Chemical and boron isotopic variations of tourmaline in the Hnilec graniterelated hydrothermal system, Slovakia: constraints on magmatic and metamorphic fluid evolution. Lithos 106, 1–11.
Johannes, W., Holtz, F., 1996. Formation of granitic magmas by dehydration melting. In: Petrogenesis and Experimental Petrology of Granitic Rocks. Springer, Berlin, Heidelberg, pp. 264–301.
Jurek, K., Hulínský, V., 1980. The use and accuracy of the ZAF correction procedure for the microanalysis of glasses. Microchim. Acta 73 (3), 183–198.
Kou, C.H., Liu, Y.X., Huang, H., Li, T.D., Ding, X.Z., Zhang, H., 2018. The Neoproterozoic arc-type and OIB-type mafic-ultramafic rocks in the western Jiangnan Orogen: Implications for tectonic settings. Lithos 312, 38–56.
Kou, C.H., Liu, Y.X., Li, T.D., Ding, X.Z., Zhang, H., Liu, Y., 2021. Petrogenesis and tectonic implications of the neoproterozoic mafic-ultramafic rocks in the western Jiangnan Orogen: Insights from in situ analysis of clinopyroxenes. Lithos 392, 106156.
Le Fort, P., Cuney, M., Deniel, C., France-Lanord, C., Sheppard, S.M.F., Upreti, B.N., Vidal, P., 1987. Crustal generation of the Himalayan leucogranites. Tectonophysics 134 (1–3), 39–57.
Lee, C.T.A., Morton, D.M., 2015. High silica granites: Terminal porosity and crystal settling in shallow magma chambers. Earth Planet. Sci. Lett. 409, 23–31.
Li, J.W., Deng, X.D., Zhou, M.F., Liu, Y.S., Zhao, X.F., Guo, J.L., 2010. Laser ablation ICPMS titanite U-Th–Pb dating of hydrothermal ore deposits: a case study of the Tonglushan Cu–Fe–Au skarn deposit, SE Hubei Province, China. Chem. Geol. 270, 56–67.
Li, X., Zhou, M., 2015. Multiple stages of hydrothermal REE remobilization recorded in fluorapatite in the Paleoproterozoic Yinachang Fe-Cu-(REE) deposit, Southwest China. Geochim. Cosmochim. Acta 166, 53–73.
Li, X.H., Li, Z.X., Ge, W.C., Zhou, H.W., Li, W.X., Liu, Y., Wingate, M.T.D., 2003. Neoproterozoic granitoids in South China: crustal melting above a mantle plume at ca. 825 Ma? Precamb. Res. 122, 45–83.
Li, X.H., Li, W.X., Li, Z.X., Lo, C.H., Wang, J., Ye, M.F., Yang, Y.H., 2009a. Amalgamation between the Yangtze and Cathaysia Blocks in South China: constraints from SHRIMP U-Pb zircon ages, geochemistry and Nd–Hf isotopes of the Shuangxiwu volcanic rocks. Precambrian Res. 174 (1–2), 117–128.
Li, X.H., Liu, Y., Li, Q.L., Guo, C.H., Chamberlain, K.R., 2009b. Precise determination of Phanerozoic zircon Pb/Pb age by multicollector SIMS without external standardization. Geochem. Geophys. Geosyst. 10, Q04010. https://doi.org/10.1029/cGC002400.

Li, X.H., Tang, G.Q., Gong, B., Yang, Y.H., Hou, K.J., Hu, Z.C., Li, Q.L., Liu, Y., Li, W.X., 2013. Qinghu zircon: A working reference for microbeam analysis of U-Pb age and Hf and O isotopes. Chin. Sci. Bull. 58, 4647–4654.
Li, X.Y., Chi, G.X., Zhou, Y.Z., Deng, T., Zhang, J.R., 2017. Oxygen fugacity of Yanshanian granites in South China and implications for metallogeny. Ore Geology Reviews 88, 690–701.
Li, Y.X., Yin, C.Q., Lin, S.F., Zhang, J., Gao, P., Qian, J.H., Xia, Y.F., Liu, J.G., 2021. Geochronology and geochemistry of bimodal volcanic rocks from the western Jiangnan Orogenic Belt: Petrogenesis, source nature and tectonic implication. Precambr. Res. 359, 106218.
Li, Z.X., Li, X.H., Kinny, P.D., Wang, J., 1999. The breakup of Rodinia: did it start with a mantle plume beneath South China? Earth Planet. Sci. Lett. 173 (3), 171–181.
Linnen, R.L., Keppler, H., 1997. Columbite solubility in granitic melts: consequences for the enrichment and fractionation of Nb and Ta in the Earth's crust. Contrib. Mineral. Petrol. 128 (2), 213–227.
Liu, X., Liang, H., Wang, Q., Ma, L., Yang, J. H., Guo, H. F., Xiong, X.L., Ou, Q., Zeng, J.P., Gou, G.N., Hao, L.L., 2022. Early Cretaceous Sn-bearing granite porphyries, A-type granites, and rhyolites in the Mikengshan–Qingxixiang–Yanbei area, South China: Petrogenesis and implications for ore mineralization. J. Asia Earth Sci., 105274.
Linnen, R.L., Pichavant, M., Holtz, F., 1996. The combined effects of fO2 and melt composition on SnO2 solubility and tin diffusivity in haplogranitic melts. Geochimica et Cosmochimica Acta 60 (24), 4965–4976.
Liu, Y.S., Hu, Z.C., Zong, K.Q., Gao, C., Gao, S., Xu, J., Chen, H.H., 2010. Reappraisement and refinement of zircon U-Pb isotope and trace element analyses by LA–ICP–MS. Chin. Sci. Bull. 55, 1535–1546.
London, D., 1987. Internal differentiation of rare-element pegmatites: Effects of boron, phosphorus, and fluorine. Geochim. Cosmochim. Acta 51 (3), 403–420.
London, D., Manning, D.A., 1995. Chemical variation and significance of tourmaline from Southwest England. Econ. Geol. 90, 495–519.
Ludwig, K.R., 2003. User's manual for Isoplot 3.00: a geochronological toolkit for Microsoft Excel.
Ludwig, K. R., 2012. Isoplot 4.15: a geochronological toolkit for Microsoft Excel. Berkeley Geochronological Center.
Lv, Z.H., Chen, J., Zhang, H., Tang, Y., 2021. Petrogenesis of Neoproterozoic rare metal granite-pegmatite suite in Jiangnan Orogen and its implications for rare metal mineralization of peraluminous rock in South China. Ore Geol. Rev. 128, 103923.
Mao, J.W., Cheng, Y.B., Chen, M.H., Pirajno, F., 2013. Major types and time–space distribution of Mesozoic ore deposits in South China and their geodynamic settings. Mineralium Deposita 48, 267–294.
Mao, J.W., Liu, P., Goldfarb, R.J., Goryachev, N.A., Pirajno, F., Zheng, W., Zhou, M.F., Zhao, C., Xie, G.Q., Yuan, S.D., Liu, M., 2021. Cretaceous large-scale metal accumulation triggered by post-subductional large-scale extension, East Asia. Ore Geology Reviews 136, 104270.
Martin, H., Smithies, R.H., Rapp, R., Moyen, J.F., Champion, D., 2005. An overview of adakite, tonalite–trondhjemite–granodiorite (TTG), and sanukitoid: relationships and some implications for crustal evolution. Lithos 79, 1–24.
Migdisov, A.A., Williams-Jones, A.E., Wagner, T., 2009. An experimental study of the solubility and speciation of the Rare Earth Elements (III) in fluoride- and chloride bearing aqueous solutions at temperatures up to 300°C. Geochim. Cosmochim. Acta 73, 7087–7109.
Miller, C.F., McDowell, S.M., Mapes, R.W., 2003. Hot and cold granites? Implications of zircon saturation temperatures and preservation of inheritance. Geology 31, 529–532.
Miller, C.F., Mittlefehldt, D.W., 1982. Depletion of light rare-earth elements in felsic magmas. Geology 10, 129–133.
Miller, C.F., Stoddard, E.F., Bradfish, L.J., Dollase, W.A., 1981. Composition of plutonic muscovite; genetic implications. The Canadian Mineralogist 19 (1), 25–34.
Möller, P., Dulski, P., Szacki, W., Malow, G., Riedel, E., 1988. Substitution of tin in cassiterite by tantalum, niobium, tungsten, iron and manganese. Geochim. Cosmochim. Acta 52, 1497–1503.
Murciego, A., Sanchez, A.G., Dusausoy, Y., Pozas, J.M., Ruck, R., 1997. Geochemistry and EPR of cassiterites from the Iberian Hercynian Massif. Mineral. Magaz. 61, 357–365.
Pan, L.C., Hu, R.Z., Wang, X.S., Bi, X.W., Zhu, J.J., Li, C., 2016. Apatite trace element and halogen compositions as petrogenetic-metallogenic indicators: Examples from four granite plutons in the Sanjiang region, SW China. Lithos 254–255, 118–130.
Peccerillo, A., Taylor, S.R., 1976. Geochemistry of Eocene calc-alkaline volcanic rocks from the Kastamonu area, northern Turkey. Contributions to mineralogy and petrology 58, 63–81.
Pichavant, M., 1981. An experimental study of the effect of boron on a water saturated haplogranite at 1 kbar vapour pressure. Contrib. Mineral. Petrol. 76, 430–439.
Pichavant, M.C., 1987. Effects of B and H2O on liquidus phase relations in the haplogranite system at 1 kbar. Am. Mineral. 72, 1056–1070.
Prowatke, S., Klemme, S., 2006. Trace element partitioning between apatite and silicate melts. Geochimica et Cosmochimica Acta 70 (17), 4513–4527.
Qi, L., Grégoire, D.C., 2000. Determination of trace elements in twenty six Chinese geochemistry reference materials by inductively coupled plasma-mass spectrometry. Geostand. Newslett. 24 (1), 51–63.
Qu, P., Li, N.B., Niu, H.C., Shan, Q., Weng, Q., Zhao, X.C., 2021. Difference in the nature of ore-forming magma between the Mesozoic porphyry Cu-Mo and Mo deposits in NE China: Records from apatite and zircon geochemistry. Ore Geology Reviews 135, 104218.
Qu, P., Yang, W., Niu, H., Li, N., Wu, D., 2022. Apatite fingerprints on the magmatic-hydrothermal evolution of the Daheishan giant porphyry Mo deposit, NE China. GSA Bulletin 134 (7–8), 1863–1876.
Resentini, A., Andò, S., Garzanti, E., Malusà, M.G., Pastore, G., Vermeesch, P., Chanvry, E., Dall'Asta, M., 2020. Zircon as a provenance tracer: Coupling Raman spectroscopy and UPb geochronology in source-to-sink studies. Chem. Geol. 555, 119828.
Richards, J.P., 2015. The oxidation state, and sulfur and Cu contents of arc magmas: implications for metallogeny. Lithos 233, 27–45.
Romer, R.L., Kroner, U., 2016. Phanerozoic tin and tungsten mineralization—tectonic controls on the distribution of enriched protoliths and heat sources for crustal melting. Gondwana Research 31, 60–95.
Rudnick, R.L., Gao, S., 2003. Composition of the continental crust. In: Rudnick, R.L. (Ed.), The Crust, Treatise in Geochemistry, 3. Elsevier, New York, pp. 1–64.
Sha, L.K., Chappell, B.W., 1999. Apatite chemical composition, determined by electron microprobe and laser-ablation inductively coupled plasma mass spectrometry, as a probe into granite petrogenesis. Geochim. Cosmochim. Acta 63, 3861–3881.
Shakerardakani, F., Li, X.H., Neubauer, F., Ling, X.X., Li, J., Monfaredi, B., Wu, L.G., 2020. Genesis of early cretaceous leucogranites in the Central Sanandaj-Sirjan zone, Iran: Reworking of Neoproterozoic metasedimentary rocks in an active continental margin. Lithos 352, 105330.
Shellnutt, J.G., Wang, C.Y., Zhou, M.F., Yang, Y., 2009. Zircon Lu–Hf isotopic compositions of metaluminous and peralkaline A-type granitic plutons of the Emeishan large igneous province (SW China): constraints on the mantle source. J. Asia Earth Sci. 35 (1), 45–55.
Shu, L.S., Wang, J.Q., Yao, J.L., 2019. Tectonic evolution of the eastern Jiangnan region, South China: new findings and implications on the assembly of the Rodinia supercontinent. Precambr. Res. 322, 42–65.
Shu, L.S., Yao, J.L., Wang, B., Faure, M., Charvet, J., Chen, Y., 2021. Neoproterozoic plate tectonic process and Phanerozoic geodynamic evolution of the South China Block. Earth Sci. Rev. 216, 103596.
Slack, J.F., Trumbull, R.B., 2011. Tourmaline as a recorder of ore-forming processes. Elements 7, 321–326.
Slack, J.F., 1996. Tourmaline associations with hydrothermal ore deposits. In: Grew, E. S., Anovitz, L.M. (Eds.), Boron: Mineralogy, Petrology and Geochemistry, Rev. Mineral, vol. 33. Mineral Soc America, Washington, DC, pp. 559–644.
Stacey, J.S., Kramers, J.D., 1975. Approximation of terrestrial lead isotope evolution by a two-stage model. Earth Planet. Sci. Lett. 26, 207–221.
Stein, H.J., Markey, R.J., Morgan, J.W., Du, A., Sun, Y., 1997. Highly precise and accurate Re-Os ages for molybdenite from the East Qinling molybdenum belt, Shaanxi Province. China. Econ. Geol. 92, 827–835.
Stepanov, A., Mavrogenes, J.A., Meffre, S., Davidson, P., 2014. The key role of mica during igneous concentration of tantalum. Contrib. Mineral. Petrol. 167(6), 1–8.
Sui, Q.L., Zhu, H.L., Sun, S.J., Chen, D.H., Zhao, X.J., Wang, Z.F., 2020. The geochemical behavior of tin and Late Cretaceous tin mineralization in South China. Acta Petrol. Sin. 36, 23–34 in Chinese with English abstract.
Sun, S.S., McDonough, W.F., 1989. Chemical and isotopic systematics of oceanic basalts: implications formantle composition andprocesses. In: Saunders, A.D., Norry, M.J. (Eds.), Magmatism in the Ocean Basalts. Geological Society Special Publication, pp. 313–345.
Sylvester, P.J., 1998. Post-collisional strongly peraluminous granites. Lithos 45 (1–4), 29–44.
Tang, Y.W., Cui, K., Zheng, Z., Gao, J.F., Han, J.J., Yang, J.H., Liu, L., 2020. LA-ICP-MS U-Pb geochronology of wolframite by combining NIST series and common lead-bearing MTM as the primary reference material: Implications for metallogenesis of South China. Gondwana Res. Res. 41, 29–50.
Tera, F., Wasserburg, G.J., 1975. Precise isotopic analysis of lead in picomole and subpicomole quantities. Analytical Chemistry 47 (13), 2214–2220.
Thomas, R., 2002. Determination of the H_3BO_3 concentration in fluid and melt inclusions in granite pegmatites by laser Raman microprobe spectroscopy. Am. Mineral. 87 (1), 56–68.
Thomas, R., Förster, H., Heinrich, W., 2003. The behaviour of boron in a peraluminous granite-pegmatite system and associated hydrothermal solutions: a melt and fluid inclusion study. Contrib. Miner. Petrol. 144 (4), 457–472.
Tian, S.H., Yang, Z.S., Hou, Z.Q., Mo, X.X., Hu, W.J., Zhao, Y., Zhao, X.Y., 2017. Subduction of the Indian lower crust beneath southern Tibet revealed by the post-collisional potassic and ultrapotassic rocks in SW Tibet. Gondwana Res. Res. 41, 29–50.
Tindle, A.G., Breaks, F.W., 1998. Oxide minerals of the Separation Rapids rare-element granitic pegmatite group, northwestern Ontario. Can. Mineral. 36, 609–635.
Trumbull, R.B., Chaussidon, M., 1999. Chemical and boron isotopic composition of magmatic and hydrothermal tourmalines from the Sinceni granite–pegmatite system in Swaziland. Chem. Geol. 153, 125–137.
Ulrich, T., Günther, D., Heinrich, C.A., 2002. The evolution of a porphyry Cu-Au deposit, based on LA-ICPMS analysis of fluid inclusions: Bajo de la Alumbrera, Argentina. Econ. Geol. 97, 1889–1920.
van Dongen, M., Weinberg, R.F., Tomkins, A.G., 2010. REE-Y, Ti, and P remobilization in magmatic rocks by hydrothermal alteration during Cu-Au deposit formation. Econ. Geol. 105, 763–776.
Wan, L., Timothy, M.K., Jin, W., Yang, J., Zeng, Z.Z., 2021. Neoproterozoic tectonics of the Jiangnan orogen: The magmatic record of continental growth by arc and slab-failure magmatism from 1000 to 780 Ma. Precambr. Res. 362, 106319.
Wang, M., Dai, C.G., Wang, X.H., Chen, J.S., Ma, H.Z., 2011a. In-situ zircon geochronology and Hf isotope of muscovite-bearing leucogranites from FJS, Guizhou Province, and constraints on continental growth of the Southern China block. Earth Sci. Front. 18, 213–223 in Chinese with English Abstract.
Wang, X.S., Gao, J., Klemd, R., Jiang, T., Zhai, Q.G., Li, J.L., Liang, X.Q., 2019. From arc accretion to continental collision in the eastern Jiangnan Orogen: evidence from two phases of S–type granites. Precambr. Res. 199–211.

Wang, X.C., Li, Z.X., Li, X.H., Li, Q.L., Zhang, Q.R., 2011b. Geochemical and Hf–Nd isotope data of Nanhua rift sedimentary and volcaniclastic rocks indicate a Neoproterozoic continental flood basalt provenance. Lithos 127, 427–440.
Wang, J.Q., Shu, L.S., Santosh, M., 2016. Petrogenesis and tectonic evolution of Lianyunshan complex, South China: Insights on Neoproterozoic and late Mesozoic tectonic evolution of the central Jiangnan Orogen. Gondwana Res. 39, 114–130.
Wang, R.C., Wu, F.Y., Xie, L., Liu, X.C., Wang, J.M., Yang, L., Lai, W., Liu, C., 2017. A preliminary study of rare-metal mineralization in the Himalayan leucogranite belts. South Tibet. Sci. China Earth Sci. 60, 1655–1663.
Wang, Y.J., Zhang, A.M., Cawood, P.A., Fan, W.M., Xu, J.F., Zhang, G.W., Zhang, Y.Z., 2013. Geochronological, geochemical and Nd–Hf–Os isotopic finger printing of an early Neoproterozoic arc-back-arc system in South China and its accretionary assembly along the margin of Rodinia. Precambr. Res. 231, 343–371.
Wang, Y.J., Zhang, Y.Z., Fan, W.M., Geng, H.Y., Zou, H.P., Bi, X.W., 2014b. Early Neoproterozoic accretionary assemblage in the Cathaysia block: geochronological, Lu–Hf isotopic and geochemical evidence from granitoid gneisses. Precambr. Res. 249, 144–161.
Wang, X.L., Zhou, J.C., Qiu, J.S., Gao, J.F., 2004. Geochemistry of the Meso– to Neoproterozoic basic–acid rocks from Hunan Province, South China: implications for the evolution of the western Jiangnan orogen. Precambr. Res. 135, 79–103.
Wang, X.L., Zhou, J.C., Qiu, J.S., Zhang, W.L., Liu, X.M., Zhang, G.L., 2006. LA-ICP-MS U-Pb zircon geochronology of the Neoproterozoic igneous rocks from Northern Guangxi Province, South China: implications for the tectonic evolution. Precambr. Res. 145, 111–130.
Wang, X.L., Zhou, J.C., Griffin, W.L., Wang, R.C., Qiu, J.S., O'Reilly, S.Y., Xu, X.S., Liu, X. M., Zhang, G.L., 2007. Detrital zircon geochronology of Precambrian basement sequences in the Jiangnan orogen: dating the assembly of the Yangtze and Cathaysia blocks. Precambr. Res. 159, 117–131.
Wang, W., Zhou, M.F., Yan, D.P., Li, J.W., 2012. Depositional age, provenance, and tectonic setting of the Neoproterozoic Sibao Group, southeastern Yangtze Block, South China. Precambr. Res. 192–195, 107–124.
Wang, J., Zhou, X.L., Deng, Q., Fu, X.G., Duan, T.Z., Guo, X.M., 2014. Sedimentary successions and the onset of the Neoproterozoic Jiangnan sub-basin in the Nanhua rift South China. Int. J. Earth Sci. 104, 521–539.
Wang, X.L., Zhou, J.C., Griffin, W.L., Zhao, G.C., Yu, J.H., Qiu, J.S., Zhang, Y.J., Xing, G. F., 2014a. Geochemical zonation across a Neoproterozoic orogenic belt: Isotopic evidence from granitoids and metasedimentary rocks of the Jiangnan orogeny, China. Precambr. Res. 242, 154–171.
Watson, E.B., Green, T.H., 1981. Apatite/liquid partition coefficients for the rare earth elements and strontium. Earth and Planetary Science Letters 56, 405–421.
Watson, E.B., Harrison, T.M., 1983. Zircon saturation revisited' temperature and composition effects in a variety of crustal magma types. Earth Planet. Sci. Lett. 64, 295–304.
Webster, J.D., Piccoli, P.M., 2015. Magmatic apatite: a powerful, yet deceptive, mineral. Elements 11, 177–182.
Wei, S.D., Liu, H., Zhao, J.H., 2018. Tectonic evolution of the western Jiangnan Orogen: Constraints from the Neoproterozoic igneous rocks in the FJS region, South China. Precambr. Res. 318 (2018), 89–102.
Weinberg, R.F., Hasalová, P., 2015. Water-fluxed melting of the continental crust: A review. Lithos 212, 158–188.
Williams-Jones, A., Migdisov, A., Samson, I., 2012. Hydrothermal mobilisation of the rare earth elements: A tale of "Ceria" and "Yttria". Elements 8, 355–360.
Wu, F.Y., Liu, X.C., Ji, W.Q., Wang, J.M., Yang, L., 2017. Highly fractionated granites: Recognition and research. Sci. China Earth Sci. 60, 1201–1219.
Wu, F.Y., Liu, X.C., Liu, Z.C., Wang, R.C., Xie, L., Wang, J.M., Ji, W.Q., Yang, L., Liu, C., Khanal, G.P., He, S.X., 2020. Highly fractionated Himalayan leucogranites and associated rare-metal mineralization. Lithos 352, 105319.
Wu, R.X., Zheng, Y.F., Wu, Y.B., Zhao, Z.F., Zhang, S.B., Liu, X.M., Wu, F.Y., 2006. Reworking of juvenile crust: Element and isotope evidence from Neoproterozoic granodiorite in South China. Precambr. Res. 146, 179–212.
Xia, Y., 1985. The Geochemical features and genesis of Heiwan River W-Sn Deposit in Guizhou. Geology of Guizhou 3, 253–262 in Chinese.
Xiang, L., Wang, R.C., Romer, R.L., Che, X.D., Hu, H., Xie, L., Tian, E.N., 2020. Neoproterozoic Nb-Ta-W-Sn bearing tourmaline leucogranite in the western part of Jiangnan Orogen: Implications for episodic mineralization in South China. Lithos 360, 105450.
Xiong, X., Keppler, H., Audétat, A., Ni, H., Sun, W., Li, Y., 2011. Partitioning of Nb and Ta between rutile and felsic melt and the fractionation of Nb/Ta during partial melting of hydrous metabasalt. Geochim. Cosmochim. Acta 75 (7), 1673–1692.
Xu, B., Jiang, S.Y., Wang, R., Ma, L., Zhao, K.D., Yan, X., 2015. Late Cretaceous granites from the giant Dulong Sn-polymetallic ore district in Yunnan Province, South China: Geochronology, geochemistry, mineral chemistry and Nd–Hf isotopic compositions. Lithos 218, 54–72.
Xue, H.M., Ma, F., Song, Y.Q., 2012. Mafic-ultramafic rocks from the FJS region, southwestern margin of the Jiangnan orogenic belt: Ages, geochemical characteristics and tectonic setting. Acta Petrol. Sin. 28 (9), 3015–3030.
Yan, C.L., Shu, L.S., Chen, Y., Faure, M., Feng, Z.H., Zhai, M.G., 2021. The construction mechanism of the Neoproterozoic S-type Sanfang-Yuanbaoshan granitic plutons in the Jiangnan Orogenic Belt, South China: Insights from geological observation, geochronology, AMS and Bouguer gravity modeling. Precambr. Res. 354, 106054.
Yao, J.L., Shu, L.S., Santosh, M., Li, J.Y., 2013. Geochronology and Hf isotope of detrital zircons from Precambrian sequences in the eastern Jiangnan Orogen: Constraining the assembly of Yangtze and Cathaysia Blocks in South China. J. Asia Earth Sci. 74, 225–243.
Yao, J.L., Shu, L.S., Santosh, M., Xu, Z.Q., 2014. Paleozoic metamorphism of the Neoproterozoic basement in NE Cathaysia: zircon U-Pb ages, Hf isotope and whole rock geochemistry from the Chencai Group. J. Geol. Soc. 171 (2), 281–297.
Yao, J.L., Shu, L.S., Cawood, P.A., Li, J.Y., 2017. Constraining timing and tectonic implications of Neoproterozoic metamorphic event in the Cathaysia Block, South China. Precambr. Res. 293, 1–12.
Yan, C., Shu, L., Faure, M., Chen, Y., Huang, R., 2019. Time constraints on the closure of the Paleo–South China Ocean and the Neoproterozoic assembly of the Yangtze and Cathaysia blocks: Insight from new detrital zircon analyses. Gondwana Research 73, 175–189.
Yang, Y.H., Wu, F.Y., Xie, L.W., Yang, J.H., Zhang, Y.B., 2011. High-precision direct determination of the 87Sr/86Sr isotope ratio of bottled Sr-rich natural mineral drinking water using multiple collector inductively coupled plasma mass spectrometry. Spectrochim. Acta, Part B 66, 656–660.
Yao, J.L., Cawood, P.A., Shu, L.S., Zhao, G.C., 2019. Jiangnan orogen, South China: a ~ 970–820 Ma Rodinia margin accretionary belt. Earth Sci. Rev. 196, 102872.
Yuan, S.D., Peng, J.T., Hu, R.Z., Li, H.M., Shen, N.P., Zhang, D.L., 2008. A precise U-Pb age on cassiterite from the Xianghualing tin-polymetallic deposit (Hunan, South China). Miner. Depos. 43, 375–382.
Yuan, S.D., Peng, J.T., Hao, S., Li, H.M., Geng, J.Z., Zhang, D.L., 2011. In situ LA-MC-ICPMS and ID-TIMS U-Pb geochronology of cassiterite in the giant Furong tin deposit, Hunan Province, South China: New constraints on the timing of tin–polymetallic mineralization. Ore Geol. Rev. 43, 235–242.
Yuan, S.D., Williams-Jones, A.E., Mao, J.W., Zhao, P.L., Yan, C., Zhang, D.L., 2018. The origin of the Zhangjialong tungsten deposit, South China: Implications for W-Sn mineralization in large granite batholiths. Economic Geology 113 (5), 1193–1208.
Zeng, L., Zhao, X., Li, X., Hu, H., McFarlane, C., 2016. In situ elemental and isotopic analysis of fluorapatite from the Taocun magnetite-apatite deposit, Eastern China: Constraints on fluid metasomatism. Am. Mineral. 101, 2468–2483.
Zhang, G.W., Guo, A.L., Wang, Y.J., Li, S.Z., Dong, Y.P., Liu, S.F., He, D.F., Cheng, S.Y., Lu, R.K., Yao, A.P., 2013. Tectonics of South China Continent and its implications. Sci. China Earth Sci. 56 (11), 1804–1828.
Zhang, X.B., Guo, F., Zhang, B., Zhao, L., Wu, Y., Wang, G.Q., Alemayehu, M., 2020. Magmatic evolution and post-crystallization hydrothermal activity in the early Cretaceous Pingtan intrusive complex, SE China: Records from apatite geochemistry. Contrib. Mineral. Petrol. 175 (4), 35.
Zhang, X.B., Guo, F., Zhang, B., Zhao, L., Wu, Y., Wang, G.Q., 2021b. Mixing of cogenetic magmas in the Cretaceous Zhangzhou calcalkaline granite from SE China recorded by in-situ apatite geochemistry. Am. Mineral. 106 (10), 1679–1689.
Zhang, R.Q., Lu, J.J., Lehmann, B., Li, C.Y., Li, G.L., Zhang, L.P., Guo, J., Sun, W.D., 2017a. Combined zircon and cassiterite U-Pb dating of the Piaotang granite-related tungsten-tin deposit, southern Jiangxi tungsten district, China. Ore Geol. Rev. 82, 268–284.
Zhang, R.Q., Lehmann, B., Seltmann, R., Sun, W.D., Li, C.Y., 2017b. Cassiterite U-Pb geochronology constrains magmatic-hydrothermal evolution in complex evolved granite systems: The classic Erzgebirge tin province (Saxony and Bohemia). Geology 45, 1095–1098.
Zhang, S., Lu, J., Zhang, R., Liang, X., Ma, D., Li, R., 2021a. Tourmaline as an indicator for late-magmatic to hydrothermal fluid evolution of the Neoproterozoic Baotan tin deposit, South China. Ore Geol. Rev. 139, 104504.
Zhang, Q., Lu, J., Zhang, R., Gao, J., Zhao, X., 2023. Early Paleozoic tin mineralization in South China: Geology, geochronology and geochemistry of the Lijia tin deposit in the Miaoershan-Yuechengling composite batholith. Ore Geol. Rev. 152, 105249.
Zhang, Y., Yang, J.H., Chen, J.Y., Wang, H., Xiang, Y.X., 2017c. Petrogenesis of Jurassic tungsten-bearing granites in the Nanling Range, South China: Evidence from whole-rock geochemistry and zircon U-Pb and Hf–O isotopes. Lithos 278, 166–180.
Zhang, S., Zhang, R., Lu, J., Ma, D., Ding, T., Gao, S., Zhang, Q., 2019. Neoproterozoic tin mineralization in South China: geology and cassiterite U-Pb age of the Baotan tin deposit in northern Guangxi. Miner. Deposita 54, 1125–1142.
Zhao, G.C., 2015. Jiangnan orogen in South China: developing from divergent double subduction. Gondwana Res. 27, 1173–1180.
Zhao, G.C., Cawood, P.A., 2012. Precambrian Geology of China. Precambr. Res. 222–223, 13–54.
Zhao, H.D., Zhao, K.D., Palmer, M.R., Jiang, S.Y., Chen, W., 2021a. Magmatic hydrothermal mineralization processes at the Yidong Tin Deposit, South China: insights from in situ chemical and boron isotope changes of tourmaline. Econ. Geol. 116, 1625–1647.
Zhao, J.H., Zhou, M.F., Yan, D.P., Zheng, J.P., Li, J.W., 2011. Reappraisal of the ages of Neoproterozoic strata in South China: no connection with the Grenvillian orogeny. Geology 39, 299–302.
Zhao, J.H., Zhou, M.F., Zhen, J.P., 2013. Constraints from zircon U-Pb ages, O and Hf isotopic compositions on the origin of Neoproterozoic peraluminous granitoids from the Jiangnan Fold Belt, South China. Contrib. Mineral. Petrol. 166, 1505–1519.
Zhao, J.H., Li, Q.W., Liu, H., Wang, W., 2018. Neoproterozoic magmatism in the western and northern margins of the Yangtze Block (South China) controlled by slab subduction and subduction-transform-edge-propagator. Earth Sci. Rev. 187, 1–18.
Zhao, K.D., Zhang, L.H., Palmer, M.R., Jiang, S.Y., Xu, C., Zhao, H.D., Chen, W., 2021b. Chemical and boron isotopic compositions of tourmaline at the Dachang Snpolymetallic ore district in South China: constraints on the origin and evolution of hydrothermal fluids. Mineral. Deposita 1–20.
Zhao, W.W., Zhou, M.F., Li, Y.H.M., Zhao, Z., Gao, J.F., 2017. Genetic types, mineralization styles, and geodynamic settings of Mesozoic tungsten deposits in South China. Journal of Asian Earth Sciences 137, 109–140.
Zheng, Y.F., Gao, P., 2021. The production of granitic magmas through crustal anatexis at convergent plate boundaries. Lithos 402–403, 106232.

Zheng, C., Xu, C., Brix, M.R., Zhou, Z., 2019. Evolution and provenance of the Xuefeng intracontinental tectonic system in South China: constraints from detrital zircon fission track thermochronology. J. Asian Earth Sci. 176, 264–273.
Zheng, Y.F., Zhang, S.B., Zhao, Z.F., Wu, Y.B., Li, X.H., Li, Z.X., Wu, F.Y., 2007. Contrasting zircon Hf and O isotopes in the two episodes of Neoproterozoic granitoids in South China: implications for growth and reworking of continental crust. Lithos 96, 127–150.
Zheng, Y.F., Wu, R.X., Wu, Y.B., Zhang, S.B., Yuan, H.L., Wu, F.Y., 2008. Rift melting of juvenile arc-derived crust: geochemical evidence from Neoproterozoic volcanic and granitic rocks in the Jiangnan Orogen, South China. Precambr. Res. 163, 351–383.
Zhou, J.C., Wang, X.L., Qiu, J.S., Gao, J.F., 2004. Geochemistry of Meso- and Neoproterozoic mafic–ultramafic rocks from northern Guangxi, China: arc or plume magmatism? Geochem. J. 38, 139–152.
Zhou, J.C., Wang, X.L., Qiu, J.S., 2009. Geochronology of Neoproterozoic mafic rocks and sandstones from northeastern Guizhou, South China: Coeval arc magmatism and sedimentation. Precambr. Res. 170 (1–2), 27–42.
Zhou, M.F., Yan, D.P., Kennedy, A.K., Li, Y., Ding, J., 2002. SHRIMP U-Pb zircon geochronological and geochemical evidence for Neoproterozoic arc-magmatism along the western margin of the Yangtze Block, South China. Earth Planet. Sci. Lett. 196 (1–2), 51–67.